



**NARSIS**

**New Approach to Reactor Safety Improvements**

## **WP2: Fragility assessment of main NPPs critical elements**

### **D2.2 - Methodology to account for cumulative effects in the fragility assessment: theoretical aspects**



This project has received funding from the Euratom research and training programme 2014-2018 under Grant Agreement No. 755439.





## Table of contents

<b>1</b>	<b>Executive Summary .....</b>	<b>6</b>
<b>2</b>	<b>Introduction .....</b>	<b>7</b>
<b>3</b>	<b>Thermo-mechanical HCF - Preliminary damage pattern.....</b>	<b>12</b>
3.1	Uniaxial Wöhler curves interpolation .....	12
3.2	Nonlinear cumulative damage law.....	15
3.3	Estimation of lifetime ratios for triaxial complex loading .....	15
3.3.1	Approach 1: triaxial proportional loading .....	16
3.3.2	Approach 2: triaxial non-proportional repetitive loading .....	17
3.4	Synthesis.....	20
<b>4</b>	<b>Nonlinear seismic response – Final damage pattern.....</b>	<b>21</b>
4.1	Elastoplastic model including isotropic damage description .....	21
4.2	Identification of material parameters .....	23
4.2.1	Parameters describing plasticity.....	24
4.2.2	Parameters describing damaging process .....	26
4.3	The LATIN-PGD solver in a nutshell .....	28
<b>5</b>	<b>Synthesis of the approach – Fragility curves.....</b>	<b>31</b>
<b>6</b>	<b>Conclusions .....</b>	<b>33</b>
<b>7</b>	<b>References.....</b>	<b>34</b>

## List of Figures

Fig. 1: Primary circuit piping element under study - Presence of SS 304L grade in a NPP reactor (from [Poulain, 2015]).	7
Fig. 2: Wöhler curves obtained for AISI 304L (THY) steel grade - Experimental data gathered from [Vincent et al., 2012, Colin et al., 2011] and collected in a single plot.	8
Fig. 3: Two damage descriptions - Micro-cracks density $D$ vs. lifetime ratio $d$ . The values in $\mu\text{m}$ correspond to characteristic length of cracks for different damage states. Colored lines represent the bijective mapping proposed for relating the two descriptions: $D = D_c d^\eta$ .	10
Fig. 4: Graphical outline of the present report.	11
Fig. 5: Wöhler curves interpolation using the NLCD relation [Chaboche and Lesne, 1988] for AISI 304L (THY) SS grade - Experimental points extracted from refs. in Table 2 and associated model predictions for different mean stress values (continuous lines).	13
Fig. 6: Thermal loading #1 - Known arbitrary loading.	16
Fig. 7: Preliminary thermal loading - Approach #1 - Computation of $dg$ for each Gauss points.	17
Fig. 8: Thermal loading #2 - Repetition of $N$ blocks composed of $P$ known phases.	19
Fig. 9: Preliminary thermal loading - Approach #2 - Computation of $dg$ for each Gauss points.	19
Fig. 10: Experimental results (blue curves) vs. best NLS fitted model predictions (red curves) for the four experimental refs. of Table 2.	25
Fig. 11: Original stored energy $wSp$ (zoom on the right).	27
Fig. 12: Corrected stored energy $wSp$ (zoom on the right).	27
Fig. 13: The mechanical domain under study.	28
Fig. 14: Iterative resolution with search directions $\mathbb{G}$ and $\mathbb{A}$ .	29
Fig. 15: Iterative strategy used for handling parametric dependency.	30
Fig. 16: Synthesis - Computation of fragility curves including nominal thermal ageing.	32
Fig. 17: Signal modelling procedure proposed in [Charbonnel, 2018].	32

## List of Tables

Table 1: Chemical composition of the THY AISI 304L austenitic SS (in % mass), from [Vincent et al., 2012]. .....	10
Table 2: Experimental references considered for identification of the THY 304L SS material parameters. ....	11
Table 3: NLCD parameters identified from experimental points of refs. collected in Table 2. The comparison between predictions $\mathcal{W}\Delta\sigma, \sigma; \theta$ and test results for different values of $\sigma$ are given in Fig. 5. ....	13
Table 4: Parameters of the new law proposed for $\mathcal{W}$ in (16) and identified from experimental points of refs. collected in Table 2. The comparison between predictions $\mathcal{W}\Delta\sigma, \sigma; \theta$ and test results for different values of $\sigma$ are given in Fig. 2.....	14
Table 5: Dual and primal internal variables used for LCF modeling. ....	21
Table 6: AISI 304L SS (THY) reliably known monotonic properties after [Colin et al., 2011; Kweon et al., 2021].	23
Table 7: Optimal plasticity parameters for AISI 304L SS w.r.t. experimental refs. In Table 2 - Nonlinear kinematic hardening with variable $\gamma p$ and $Cp$ - Power and exponential law for isotropic hardening.....	26
Table 8: Optimal damage parameters for AISI 304L SS with respect to experimental refs. In Table 2 – To be used with isotropic hardening power law (39).....	28

## 1 Executive Summary

The present contribution aims at developing a methodology for characterizing the probabilistic behaviour of a critical Nuclear Power Plant (NPP) component (e.g., piping device) submitted to two kinds of sequential loading: *(i)* a preliminary High-Cycle Fatigue (HCF) thermo-mechanical loading, considered for nominal lifetime calculation, and *(ii)* a damaging seismic accidental ground motion. The main challenge of this work resides in gathering the probabilistic modelling tools, classically used for HCF- and seismic- risk assessment, in a unifying framework with the objective of deriving the so-called multi-input or vector-valued fragility curves describing the conditional probability (called probability of failure) that one of the mechanical states of the studied structure exceeds a given threshold value and this, as a function of both *(i)* the duration of the nominal phase at the beginning of the accident and *(ii)* the intensity of the likely seismic input.

In this report, we describe the methodology derived for simulating the damaging process of an elastoplastic component submitted to a seismic event consecutive to a preliminary HCF nominal loading. A unifying Low-Cycle Fatigue (LCF)/HCF damage description is proposed and an innovative Model Order Reduction (MOR)-based strategy is defined for an efficient simulation of the multiple load cases defining the seismic scenario. All the material parameters associated to Thyssen (THY) AISI 304L stainless-steel required for conducting this analysis are identified from experimental results in this contribution.

## 2 Introduction

The European H2020 research project NARSIS focuses on the development of methodologies for Probabilistic Safety Assessment (PSA) of NPPs against external natural hazards, in the light of the 2011 Fukushima Dai-ichi nuclear accident, which has stressed the necessity of conducting multi-factorial risk analyses for NPPs. In this contribution, both nominal thermal loading and accidental seismic risk are considered in a consecutive manner.

The component proposed for study in this deliverable is a primary-circuit piping element made of 304L grade austenetic Stainless-Steel (SS) subjected to both HCF thermomechanical loading and seismic risk (see Fig. 1).

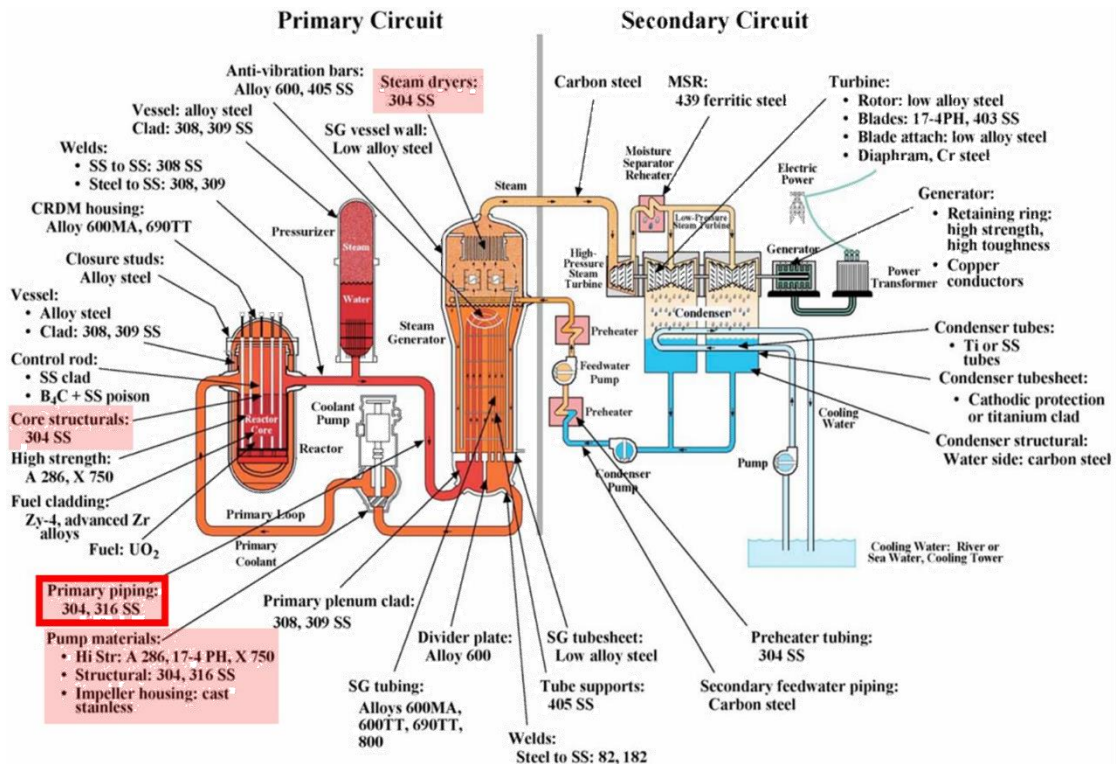


Fig. 1: Primary circuit piping element under study - Presence of SS 304L grade in a NPP reactor (from [Poulain, 2015]).

Associated uncertainties, especially regarding the load conditions are huge. Indeed, when considering seismic events, neither the time of occurrence nor the characteristics of the potential seismic input are known. Under nominal operating conditions, the system is brought to endure up to millions of load cycles, which exact number is of course unknown, especially knowing that this one might be conditioned by the occurrence of an earthquake. In other words, none of the preliminary nominal thermo-mechanical phase, during which the system undergoes fatigue phenomena, nor external seismic motion input are known in a deterministic manner, which stresses the importance of resorting to probabilistic approaches. Moreover, the material properties themselves are also affected by uncertainties. Considering the large number of simulations required for taking those uncertainties into account for safety analysis purposes, it is thus necessary to resort to a numerically attractive strategy capable of handling different cumulative damaging processes.

Regarding fatigue phenomena, several regimes may be classically distinguished, depending on the load profile and expected *number of cycles to rupture*, denoted  $N_R$ . Low-Cycle Fatigue (LCF) is considered when structures are submitted to heavy load cycles, which induce irreversible (plastic) strains at small or large scale, giving rise to damage up to crack initiation and propagation. The number of cycles to failure for LCF applications is generally low ( $N_R < 10^4$ ). High-Cycle Fatigue (HCF) in turn is considered when the load cycles induce stresses

close to, but below engineering yield stress, so that the number of cycles to initiate cracks at meso-scale is ‘higher’ (classically  $N_R > 10^5$ ). The plastic strain is usually not measurable on a meso-scale but dissipation exists on a micro-scale precisely inducing the damage phenomenon.

Regarding HCF, for a given material, the key reference-data are contained in the *Wöhler curves* (see e.g. [Lee et al. 2011, Pedersen, 2018] or [Lemaitre and Desmorat, 2005, chap.6] for an introduction). These curves are obtained experimentally after submitting a given specimen to a, often uniaxial, imposed sinusoidal loading in terms of stress or strain. These tests are conducted on several samples of the same specimen to account for variability as illustrated in Fig. 2.

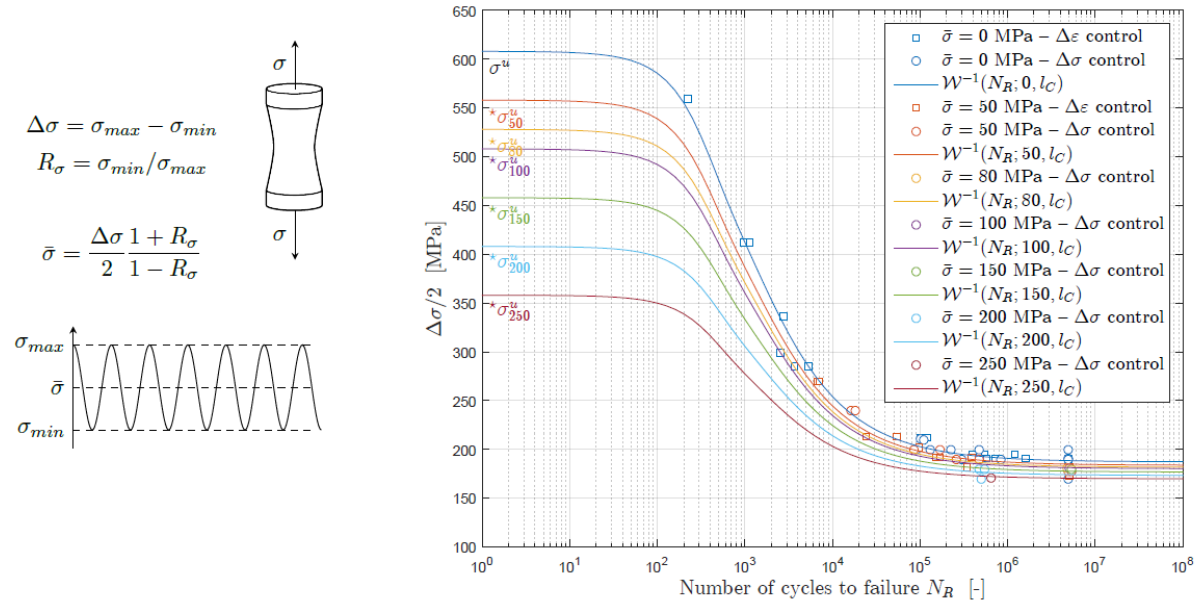


Fig. 2: Wöhler curves obtained for AISI 304L (THY) steel grade - Experimental data gathered from [Vincent et al., 2012, Colin et al., 2011] and collected in a single plot.

Different configurations are considered for assessing the effect of the load-amplitude  $\Delta\sigma$  and mean stress  $\bar{\sigma}$  on the observed number  $N_R$  of cycles before rupture. The latter can be described symbolically under the form:

$$N_R = \mathcal{W}(\Delta\sigma, \bar{\sigma}; l_C) + w \quad (1)$$

introducing the random variable  $w$ , whose  $\log_{10}$  distribution is generally assumed to be Gaussian, and a nonlinear function  $\mathcal{W}$  parameterized by a *failure criterion*  $l_C$ . Please note that Wöhler curves characterize the fatigue resistance of materials, but from a macro-scale point of view. The failure criterion  $l_C$  is generally associated to a characteristic ‘unacceptable’ crack length at the macro-scale. Of course, this characteristic length  $l_C$ , or any other criterion, is material-dependent but might also vary depending on the application (automotive, aeronautics, military application, nuclear safety, etc. where tolerances may be different). From  $N_R$ , a first definition of damage  $d$  can be expressed as a *lifetime ratio*, considering that the specimen has been submitted to a current number  $N$  of load cycles:

$$d = \frac{N}{N_R} \quad (2)$$

For lifetime evaluation of specimens submitted to general not-necessary periodical load profiles  $\sigma(t)$ , one relies on *cycle counting methods* such as *rainflow count* [see e.g. [Lee and Tjhung, 2011]] for establishing the number of cycles  $N^{(i)}$  performed at a given amplitude/mean

stress range  $(\Delta\sigma^{(i)}, \bar{\sigma}^{(i)})$ . From the different regimes  $(i)$  characterized in a reference Wöhler curve, one can access to the  $N_R^{(i)}$  and then estimate the associated damage as  $d^{(i)} = N^{(i)}/N_R^{(i)}$ . Final damage (interpreted as a lifetime ratio) can then be obtained using linear or nonlinear cumulative laws [Chaboche and Lesne, 1988; Dang Van and Paradopoulos, 1999; Lemaitre et al., 2009, Lee et al., 2011].

Regarding LCF, the damage state associated to a given load pattern is generally evaluated in the continuum damage mechanics framework. When isotropic damage is considered [Lemaitre and Desmorat, 2005], the scalar damage variable, that will be denoted  $D$  in this contribution, describes a density of micro-cracks in a Reference Elementary Volume (REV) in such a manner that the *effective stress tensor*  $\tilde{\sigma}$  writes:

$$\tilde{\sigma} = \frac{\sigma}{(1 - D)} \quad (3)$$

Damage evolution is governed by plasticity and described by e.g., Lemaitre's law up to critical value  $D_c$  where failure is supposed to occur. Many lifetime predictions have been computed using such damage description in various fields of applications (automotive, aerospace, civil engineering, etc.), involving different kinds of materials (metallic alloys but also concrete) and this, using isotropic or anisotropic damage description. Simulation durations can be long for industrial applications, especially when parametric studies are to be considered. For the purpose of LCF predictions, many developments involving the LATIN-PGD methodology have been derived since its introduction in the eighties [Ladevèze, 1985]. The LARge-Time INcrement method (LATIN) is a non time-incremental iterative strategy developed for computing solutions of nonlinear problems in mechanics in a sequence of so-called *linear* and *nonlinear* stages. The method relies on a *low rank approximation* called Proper Generalized Decomposition (PGD), sometimes referred to as Model Order Reduction (MOR) technique, for solving the linear stages in a computationally attractive manner. The LATIN methodology has been applied in various fields including continuum damage mechanics for fatigue prediction [Cognard and Ladevèze, 1993, Arzt and Ladevèze, 1994]. Most recent developments for LCF [Alameddin et al., 2017; Bhattacharyya et al., 2018a, Bhattacharyya et al., 2018b, Bhattacharyya et al., 2019] proposed a first implementation of the PGD for these problems to enable faster resolution. For earthquake engineering purpose, a first application of the LATIN-PGD methodology has been proposed during the doctoral work of Sebastian Rodriguez-Iturra (NARSIS WP4). In addition to adapting the general LATIN-PGD resolution to the framework of low frequency dynamics, an efficient time multi-scale strategy was derived to further improve the performance of the algorithm during the linear stage. This work will also rely on the numerical efficiency of the MOR-based LATIN-PGD framework for computing the LCF seismic response of an elastoplastic piping component.

Indeed, in this contribution, the objective is to evaluate the damage state of a metallic piping element submitted to a preliminary HCF loading of thermal origin followed by an imposed seismic ground motion. The study of the preliminary thermal phase will be conducted using HCF approaches involving lifetime ratio damage description (2) and Wöhler curves interpolation based methods. The seismic response of the piping element, in turn, will be computed under LCF assumption and in the continuum damage mechanics framework using damage description (3). Let us stress that the damage pattern  $d(x_g, t_s)$  at each Gauss point of the discretized model caused by the preliminary thermal loading is an input of the seismic problem at time  $t_s$  of occurrence of the ground motion (see Fig. 4). A particular attention must be paid for harmonizing the two currently used damage descriptions  $d$  (HCF) and  $D$  (LCF). Fig. 3 gives an illustration of the bijective mapping between  $d$  and  $D$  that is assumed and modeled in this work.

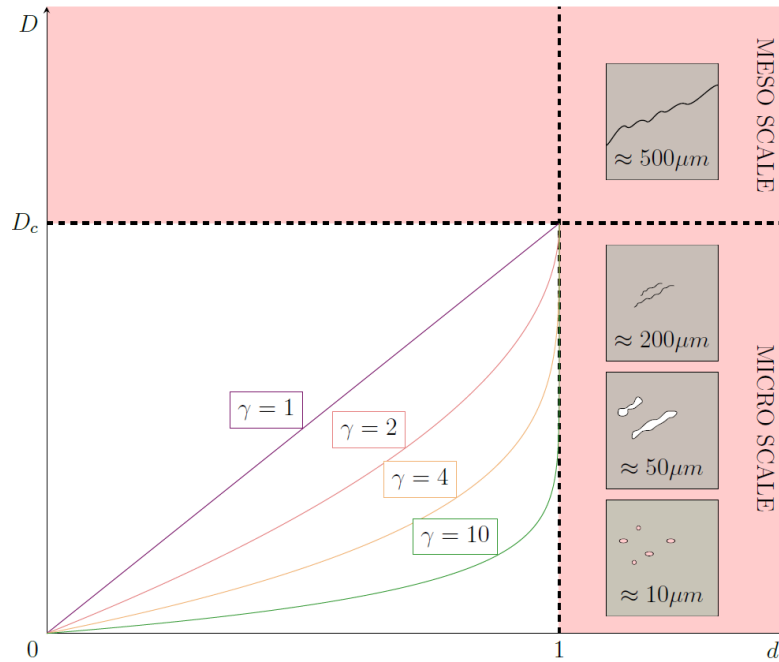


Fig. 3: Two damage descriptions - Micro-cracks density  $D$  vs. lifetime ratio  $d$ . The values in  $\mu\text{m}$  correspond to characteristic length of cracks for different damage states. Colored lines represent the bijective mapping proposed for relating the two descriptions:  $D = D_c d^\gamma$ .

We have chosen to focus on AISI austenetic 304L stainless steel (SS) because it is mostly used in the nuclear industry (see Fig. 1) and one of the objective of this deliverable is to identify all the material parameters required for conducting the combined HCF/LCF risk analysis from experimental references.

In this work, characteristics of Thyssen (THY) 304L SS grade is considered (see Table 1 for chemical composition).

Table 1: Chemical composition of the THY AISI 304L austenitic SS (in % mass), from [Vincent et al., 2012].

Name	C	Mn	Si	S	P	Ni	Cr	Mo	Cu	N	Fe
THY	0.023	1.13	0.49	0.004	0.024	10.1	18.5	0.09	0.1	0.028	Bal.

Despite numerous requests to the various actors of the NARSIS project, no experimental data on 304L SS was provided and only open-access references, as collected in Tab. 2, could have been considered as reference for identification. More reliable material parameters values could have possibly been obtained if a broader and richer experimental database could have been consulted. However, such experimental references was sufficient for tuning LCF model and HCF charts with satisfying predictability capabilities (to a certain extent), which was one of the objectives of present work.

Hence, the objectives of the preliminary work presented in this contribution consist in:

- (O1) identifying the parameters contained in vector  $\theta$  describing the Wöhler charts  $\Delta\sigma/2 = \mathcal{W}^{-1}(N_R; \bar{\sigma}, \theta)$  from experimental data (see Fig. 2);
- (O2) identifying the material parameters contained in vector  $\eta$  of a damageable elastoplastic model from reference experimental tests  $[T, C10, C1, C2]$  collected in Table 2;
- (O3) deriving a rigorous methodology for handling preliminary HCF fatigue of thermal origin followed by dynamical seismic loading.

Table 2: Experimental references considered for identification of the THY 304L SS material parameters.

Designation	Test description	Refs.
[T]	Uniaxial tension test	[Kweon et al., 2021]
[C10]	Uniaxial cyclic test (10 cycles)	[Kpodekon et al., 2009]
[C1]	LCF test – $\Delta\varepsilon$ control – $N_R = 221$	[Colin et al., 2011]
[C2]	LCF test – $\Delta\varepsilon$ control – $N_R = 975$	[Colin et al., 2011]
[–]	HCF tests (see Fig. 2)	[Vincent et al., 2012, Colin et al., 2011]

Fig. 4 gives a graphical outline of this contribution, which is structured in order to detail how the above-mentioned objectives are met.

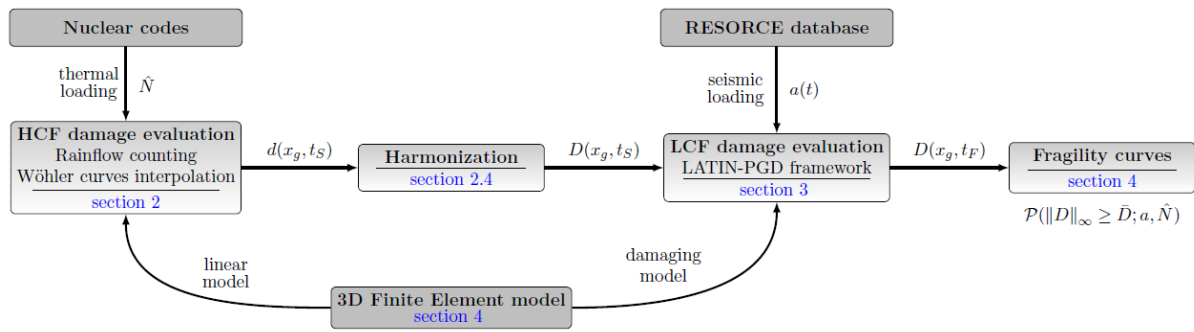


Fig. 4: Graphical outline of the present report.

Thus, section 3 is dedicated to the evaluation of the damage pattern  $d(x_g, t_S)$  produced by the HCF thermal loading. This field has to be evaluated for each Gauss point  $x_g$  of a given Finite-Element (FE) model, at time  $t_S$  when a potential earthquake occurs. Time of occurrence  $t_S$  is directly related to the number of cycles endured during the nominal phase. The parameters  $\theta$  describing the Wöhler curves  $\Delta\sigma/2 = \mathcal{W}^{-1}(N_R; \bar{\sigma}, \theta)$  for uniaxial sinusoidal loading are first identified from test results in [Colin et al., 2011, Vincent et al., 2012]. An extension for estimating lifetime ratio under sinusoidal triaxial loading from behavior is then proposed; several avenues can be considered and are described in section 3. The case of more complex non-necessarily sinusoidal loading is also addressed, involving rainflow counting methods and further assumptions on the loading itself, leading to the targeted damage field  $d(x_g, t_S)$ .

Seismic analysis in turn, is detailed in section 4. Given the initial HCF damage, the structural response of the piping element under study will be evaluated using the LATIN-PGD framework. The nonlinear damaging model used for seismic application will be detailed in a rigorous thermodynamical framework and associated material parameters will be identified from various tests results. A whole family of potential seismic inputs, characterizing a virtual seismic hazard scenario, will be defined as inputs of the nonlinear FE damaging model. Section 4 will especially highlight why the LATIN-PGD strategy and its reduced bases are particularly adapted to the multiple evaluation of similar structures.

Section 5 will give a synthesis of the main contributions as well as further details on the manner the results are collected for building the so-called fragility curves, which aims at computing the probability  $\mathcal{P}(\|D\|_\infty \geq \bar{D}; a, \hat{N})$  that the maximum damage state  $\|D\|_\infty$  exceeds a given threshold  $\bar{D}$  and this as a function of the maximal amplitude  $a$  of the potential seismic input and of the number of preliminary thermal load cycles  $\hat{N}$  endured by the structural element in the nominal phase.

Section 6 finally gives conclusions.

### 3 Thermo-mechanical HCF - Preliminary damage pattern

In this section a methodology for estimating the damage pattern on a structure submitted to triaxial loading is described, using Wöhler curves as experimental reference. A first natural definition, see eq. (2), describes damage as lifetime ratio  $d$  for a given specimen undergoing load cycles of known amplitude. The failure of the specimen is considered at the macro-scale (apparition of pre-rupture cracks of characteristic length  $l_c$ , see Fig. 2) and concerns specimens submitted to uniaxial loading. This formulation defines the damage increment per cycle  $\delta d/\delta N$  as  $1/N_R$  to yield:

$$\delta d = \underbrace{[\mathcal{W}(\Delta\sigma, \bar{\sigma}; \boldsymbol{\theta})]^{-1}}_{N_R} \delta N \quad (4)$$

Now integrating this relation on the whole load duration to rupture leads to the definition of  $N_R$  eq. (1). Subsection 3.1 details the chosen representation for  $\mathcal{W}$  and explains how parameters  $\boldsymbol{\theta}$  are identified. If one now considers, for a block  $i$  made of  $N_i$  cycles of a multi-level loading, with amplitude  $\Delta\sigma_i$  and mean stress  $\bar{\sigma}_i$ , one can write:

$$\int_{d_{i-1}}^{d_i} \delta d = [\mathcal{W}(\Delta\sigma_i, \bar{\sigma}_i; \boldsymbol{\theta})]^{-1} \int_0^{N_i} \delta N = \frac{N_i}{N_R^i} \quad (5)$$

to yield, after summation, the well-known Miner's linear rule for accumulation of damage:

$$d = \sum_i \frac{N_i}{N_R^i} \quad (6)$$

The application of such cumulative rules from simple sinusoidal uniaxial loading to more complex triaxial loading is not straightforward; the proposed answer is described in details in subsection 3.3. Subsection 3.4 draws a synthesis of the proposed approach. A first step will then consist in predicting the number of cycle to rupture  $N_R$  for given load conditions  $(\Delta\sigma, \bar{\sigma})$  with  $\Delta\sigma/2 = \mathcal{W}^{-1}(N_R; \bar{\sigma}, \boldsymbol{\theta})$ . This is the purpose of upcoming section 3.1 where different descriptions  $\mathcal{W}$  are tested and associated parameters  $\boldsymbol{\theta}$  identified.

#### 3.1 Uniaxial Wöhler curves interpolation

A first attempt to model the Wöhler relation  $\mathcal{W}$ , following the lines of [Chaboche and Lesne, 1988], is presented. This approach, called Non-Linear Continuous fatigue Damage (NLCD), consists in modelling the damage increment per cycle as:

$$\frac{\delta d}{\delta N} = \frac{\sigma^M - \sigma^\infty(\bar{\sigma})}{\sigma^U - \sigma^M} \left[ \frac{\sigma^M - \bar{\sigma}}{B_0(1 - b\bar{\sigma})} \right]^\beta \quad (7)$$

introducing ultimate tensile stress  $\sigma^U$ , three constant parameters  $b, \beta, B_0$  and the fatigue limit stress  $\sigma^\infty(\bar{\sigma})$ , that can be classically described as an affine function of the mean stress under the form:

$$\sigma^\infty(\bar{\sigma}) = \bar{\sigma} + \sigma_0^\infty(1 - b\bar{\sigma}) \quad (8)$$

where  $\sigma_0^\infty$  is the fatigue limit under reversed stress conditions ( $\bar{\sigma} = 0$ ). Note that the denominator  $B_0(1 - b\bar{\sigma})$  in eq. (7) is built according to the same affine dependency between fatigue limit and mean stress. Integrating (7) for  $d \in [0, 1]$  and  $N \in [0, N_R]$  leads to describe the number of cycles to rupture as:

$$N_R = \mathcal{W}(\Delta\sigma, \bar{\sigma}; \boldsymbol{\theta}) = \frac{\sigma^U - \sigma^M}{\sigma^M - \sigma^\infty(\bar{\sigma})} \left[ \frac{\sigma^M - \bar{\sigma}}{B_0(1 - b\bar{\sigma})} \right]^{-\beta} \quad (9)$$

involving the five parameters contained in vector  $\boldsymbol{\theta} = (\sigma^U; \sigma_0^\infty; B_0; b; \beta)$ .

Using the reference test-data of Table 2 and identifying the parameters in  $\theta$  in the non-linear least-squares sense leads to the coefficients in Table 3. Experimental points of refs. collected in Table 2 and predictions brought by relation (9) for different values of  $\bar{\sigma}$  are compared on Fig. 5.

Table 3: NLCD parameters identified from experimental points of refs. collected in Table 2. The comparison between predictions  $\mathcal{W}(\Delta\sigma, \bar{\sigma}; \theta)$  and test results for different values of  $\bar{\sigma}$  are given in Fig. 5.

$\sigma^u$	608 MPa
$\sigma_0^\infty$	190 MPa
$b$	$3.88 \times 10^4 \text{ MPa}^{-1}$
$B_0$	$2.89 \times 10^5 \text{ MPa}$
$\beta$	1.073
<b>Relative LS error</b>	<b>4.58%</b>

One can notice from Fig. 5 that the relation  $\mathcal{W}$  enables a good reproduction of the HCF behavior, whereas some experimental LCF points seem to be above model prediction. Let one stress that the relation is expressed under small perturbation assumption, involving classical ‘engineering stress/engineering strain’. Different coefficients for this relation can be found in [Lemaitre et al., 2009, p.342, Tab. 8.3] but seem to be associated to a ‘true-stress/true-strain’ description.

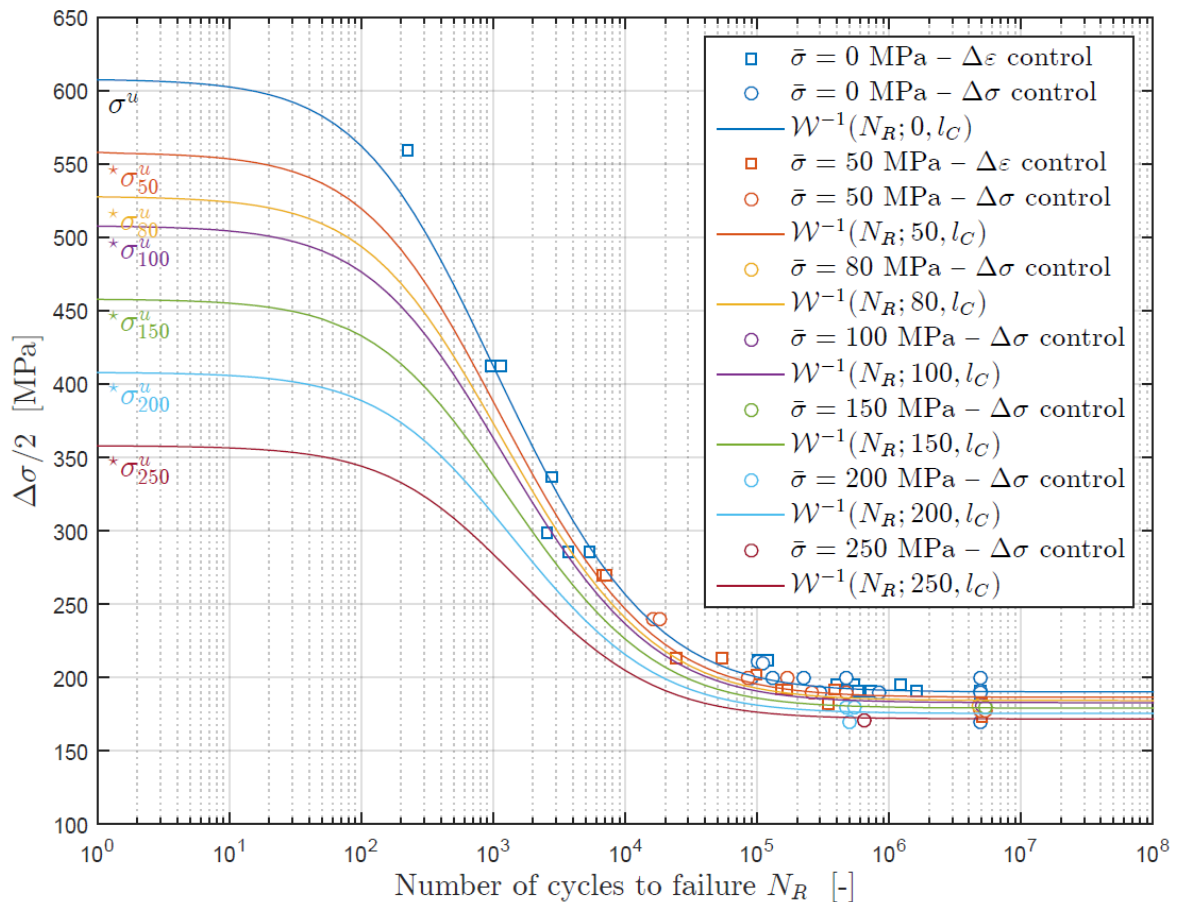


Fig. 5: Wöhler curves interpolation using the NLCD relation [Chaboche and Lesne, 1988] for AISI 304L (THY) SS grade - Experimental points extracted from refs. in Table 2 and associated model predictions for different mean stress values (continuous lines).

Alternatively, in this contribution, a new empirical law is defined and tested, in order to improve the LCF predictions as described hereafter. The relation  $\mathcal{W}$  is expressed using simple trigonometric functions and hyperbolic sines:

$$\frac{\Delta\sigma}{2} = \mathcal{W}^{-1}(N_R; \bar{\sigma}, \boldsymbol{\theta}) = A \tan^{-1}(-\psi_c(n - n_0)) + \sigma_0 \quad (10)$$

with  $n = \log_{10}(N)$  and:

$$\psi_c(x) = \begin{cases} c \sin(x/c) \\ c \sinh^{-1}(x/c) \end{cases} \quad (11)$$

The constants  $A$  and  $\sigma_0$  must satisfy the two ultimate and infinity loading conditions:

$$\begin{aligned} \left. \frac{\Delta\sigma}{2} \right|_{N=1} &= {}^* \sigma^U = \sigma^U - \bar{\sigma} \\ \left. \frac{\Delta\sigma}{2} \right|_{N=\infty} &= \sigma^\infty - \bar{\sigma} = \sigma_0^\infty (1 - b\bar{\sigma}) \end{aligned} \quad (12)$$

Taking those conditions into account leads to:

$$\frac{\Delta\sigma}{2} = A [\tan^{-1}(-\psi_c(n - n_0)) - \tan^{-1}(-\psi_c(-n_0))] + {}^* \sigma^U \quad (13)$$

with:

$$A = \frac{\sigma^U - \sigma^\infty(\bar{\sigma})}{\Pi/2 + \tan^{-1}(-\psi_c(-n_0))} \quad (14)$$

and:

$$\sigma^\infty(\bar{\sigma}) = \bar{\sigma} + \sigma_0^\infty (1 - b\bar{\sigma}) \quad (15)$$

Note that relations (13) to (15) involve five parameters contained in vector  $\boldsymbol{\theta} = (\sigma^U; \sigma_0^\infty; n_0; c; b)$  and can be easily inverted to yield:

$$N_R = \mathcal{W}(\Delta\sigma, \bar{\sigma}; \boldsymbol{\theta}) = 10^{n_0 - \psi_c^{-1}\left(\tan\left(\frac{\Delta\sigma/2 - {}^* \sigma^U}{A}\right) + \tan^{-1}(-\psi_c(-n_0))\right)} \quad (16)$$

Once again, the five parameters are identified by non-linear least squares inversion and are collected in Table 4. Fig. 2 compares the predictions  $\mathcal{W}(\Delta\sigma, \bar{\sigma}; \boldsymbol{\theta})$  with experimental points of refs. collected in Table 2, for different values of  $\bar{\sigma}$ . One can notice that this new empirical law behaves better in the LCF range and achieves lower relative error level with the same number of parameters.

Table 4: Parameters of the new law proposed for  $\mathcal{W}$  in (16) and identified from experimental points of refs. collected in Table 2. The comparison between predictions  $\mathcal{W}(\Delta\sigma, \bar{\sigma}; \boldsymbol{\theta})$  and test results for different values of  $\bar{\sigma}$  are given in Fig. 2.

$\sigma^U$	608 MPa
$\sigma_0^\infty$	187 MPa
$b$	$3.71 \times 10^4 \text{ MPa}^{-1}$
$c$	1.47
$n_0$	3.07
<b>Relative LS error</b>	<b>3.77%</b>

### 3.2 Nonlinear cumulative damage law

As already explained at the beginning of section 3, relations written such as (4) for modelling the damage increment  $\delta d/\delta N$  per cycle only enable to recover Miner's linear damage accumulation rule which might be too conservative. What the authors advocate in [Chaboche and Lesne, 1988] is to include a dependency on  $d$  in the damage increment as follows:

$$\frac{\delta d}{\delta N} = d^\alpha \left[ \frac{\sigma^M - \bar{\sigma}}{a^{1/\beta} B_0 (1 - b\bar{\sigma})} \right]^\beta \quad (17)$$

where  $\alpha$  is a function of the loading such as:

$$\alpha = 1 - a \left\langle \frac{\sigma^M - \sigma^\infty(\bar{\sigma})}{\sigma^U - \sigma^M} \right\rangle \quad (18)$$

introducing a new scalar  $a$ . No test results were consulted for rigorous experimental identification of  $a$  but values within [0.2; 0.9] seem to be appropriate for AISI 304L SS [Lemaitre et al., 2009]. Integrating this last expression for  $d \in [0; 1]$  and  $N \in [0; N_R]$  leads to the same expression (9) for the number of cycle to failure  $N_R$ . However, for periodic loading defined by constant  $(\Delta\sigma, \bar{\sigma})$ , the current damage value  $d$  after  $N$  cycles writes:

$$d = \left( \frac{N}{N_R} \right)^{\frac{1}{1-\alpha}} \quad (19)$$

and for several blocks containing  $N_i$  cycles of load characteristics  $(\Delta\sigma_i, \bar{\sigma}_i)_i$ , a non-linear cumulative damage rule is obtained:

$$d = \sum_i \left( \frac{N_i}{N_R^i} \right)^{\frac{1}{1-\alpha}} \quad (20)$$

Furthermore, when defining a new damage variable  $d^*$  using a bijective change of variable such that  $d^* = \phi(d)$  and such that  $\phi(0) = 0$  and  $\phi(1) = 1$ , one can define the damage increment as:

$$\frac{\delta d}{\delta N} = \frac{(\phi(d))^\alpha}{k\phi'(d)} \left[ \frac{\sigma^M - \bar{\sigma}}{a^{1/\beta} B_0 (1 - b\bar{\sigma})} \right]^\beta \quad (21)$$

where  $k$  is a new constant, to obtain an alternative cumulative damage law:

$$d = \sum_i \phi^{-1} \left( \left( \frac{N_i}{N_R^i} \right)^{\frac{1}{1-\alpha}} \right) \quad (22)$$

For example, when referring to Fig. 3, the mapping  $\phi(d) = d^\eta$  can be used, leading to  $\phi^{-1}(d^*) = d^{*1/\eta}$ .

Both nonlinear cumulative damage rules expressed in (7) and (17) can be used in lieu and place of the (sometimes too conservative) linear Miner's rule (6).

### 3.3 Estimation of lifetime ratios for triaxial complex loading

From now on, only sinusoidal unidirectional loading of known load characteristics  $(\Delta\sigma, \bar{\sigma})$  have been considered. Methods, based on predicting the number of cycles to rupture for elementary periodical loading, were given for estimating damage. With the objective evaluating structures, such as primary-circuit piping devices, where the stress tensor  $\sigma(x, t)$  in each point  $x$  and at

each time  $t$ , cannot be assumed to be unidirectional, additional developments are needed. Considering more complex triaxial load-cases is the purpose of current subsection.

Unfortunately, no general methodology suited to any arbitrary triaxial stress-state  $\sigma(x, t)$  has been found. However, two approaches, requiring a few hypothesis on the loading, have been derived and are presented below.

### 3.3.1 Approach 1: triaxial proportional loading

In this first approach, it is assumed that the thermal loading can take any arbitrary values but is known in a deterministic manner (see Fig. 6). Additionally, one assumes that the thermal loading generates for the studied structure a constant stress state distribution; one talks about proportional loading. More precisely, from a FE perspective, at each Gauss point  $x_g$ , for each time  $t$ , the stress tensor  $\sigma(x_g, t)$  will be assumed to be proportional to a constant time-independent tensor  $\Sigma_g$  such that:

$$\sigma(x_g, t) = \Sigma_g \sigma_g(t) \quad (23)$$

where  $\sigma_g(t)$  is a scalar function of time potentially different from one Gauss point to another. Note that the matrix  $\Sigma_g$  must be normalized in some manner. In this work, we choose  $(\Sigma_g)_{eq} = 1$ , using the equivalent Von Mises stress  $(\cdot)_{eq}$ .

This last hypothesis is rather restrictive: it could correspond to the case of an elliptic thermomechanical problem with for example a rise in temperature and thermal expansion of the medium submitted to constant mechanical and flux boundary conditions. Note that for example, no parabolic thermo-mechanical problem can be treated using this approach since it would defeat hypothesis (23). The thermal fluctuations considered must guarantee that the hypothesis (23) holds, by imposing for example that the thermal flux or temperature boundary conditions are applied in a synchronous manner. In other words, transient variations of the thermal loading must be expressed using a single real-valued function  $f(t)$ .

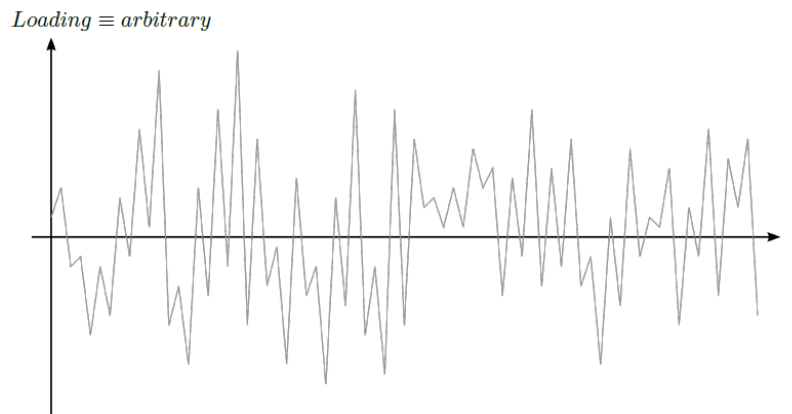


Fig. 6: Thermal loading #1 - Known arbitrary loading.

Once the thermo-mechanical problem is solved, the proportional stress distribution  $\Sigma_g \sigma_g(t)$  is known for each Gauss point. The problem being linear and stationary, only one FE computation is needed for accessing to the initial stress field  $\Sigma_g \sigma_g(t_0)$ , the complete stress time histories is proportional to  $f(t)$ . For each Gauss point, the signal  $\sigma_g(t)$  can now be decomposed using rainbow counting method that gives access to the different number of cycles  $(N_i)_i$  endured under corresponding load characteristics  $(\Delta \sigma_g^i, \bar{\sigma}_g^i)_i$ .

One can then use the charts identified in section 3.1, compute the different number of cycles to rupture  $N_R^i = \mathcal{W}(\Delta \sigma_g^i, \bar{\sigma}_g^i; \theta)$  and characterize the damage state as  $d_g^i = N_i / N_R^i$ . Final damage value is then computed using one of the previously described damage cumulative laws (6) or (20). For Miner's cumulative law, we have for each Gauss point:  $d_g = \sum_i d_g^i$ .

This first approach to the HCF damage evaluation is summed up in Fig. 7.

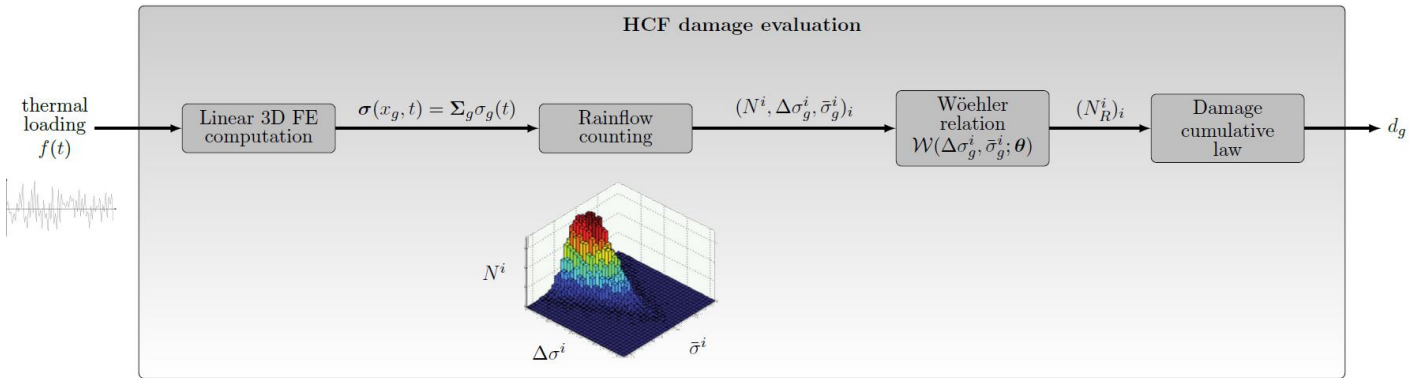


Fig. 7: Preliminary thermal loading - Approach #1 - Computation of  $d_g$  for each Gauss points.

### 3.3.2 Approach 2: triaxial non-proportional repetitive loading

A second approach is now proposed to relax the too restrictive proportional loading hypothesis (23). As explained in section 3.3.1, having such a stress-state at the Gauss points level implies that the loading can be described by a unique time function  $f(t)$  and that no transient phenomenon can modify the stress pattern  $\Sigma_g$ .

In this second approach, we consider the thermal loading to be described by a given number of independent functions contained in a vector  $f(t)$  and enable transient thermal phenomena (conduction for example) to occur such that the stress-state in the continuous medium can take any arbitrary values (stress tensor of rank 6) relaxing the proportional loading hypothesis.

The Wöhler charts  $\mathcal{W}(\Delta\sigma, \bar{\sigma}; \theta)$  identified in section 3.1 for unidimensional sinusoidal loading cannot be used in a straightforward manner anymore. However, a triaxial extension can be defined using the amplitude of the *octahedral shear stress* and the *mean hydrostatic stress* following the general idea proposed by [Sines, 1959]. Let here recall that in the uniaxial case, the fatigue limit is expressed as:

$$\frac{\Delta\sigma}{2} \leq \sigma_0^\infty (1 - b\bar{\sigma}) \quad (24)$$

where irreversibility limit stress at the right of the inequation has the classical affine dependency in the mean stress level  $\bar{\sigma}$ . Based on the observation that, for a vast range of metals submitted to many different load conditions, the mean shear stress has no effect on the tension fatigue limit nor on the torsion fatigue limit, whereas mean stress has a linear influence on the fatigue limit in tension and in torsion, Sines proposed a triaxial fatigue limit criterion involving the *octahedral shear stress*  $A_{II} = \frac{1}{2}(\Delta\sigma')_{eq}$  and the *mean hydrostatic stress*  $\bar{\sigma}_H$  for respectively playing the role of  $\Delta\sigma/2$  and  $\bar{\sigma}/3$ :

$$\frac{1}{2}(\Delta\sigma')_{eq} \leq \sigma_0^\infty (1 - 3b\bar{\sigma}_H) \quad (25)$$

where  $\star'$  and  $\star_H$  stand for the deviatoric and hydrostatic parts of tensor  $\star$ .

Considering a medium studied on the time-interval  $D_t = [0, T]$  with non-proportional loading stress-state, the *octahedral shear stress*  $A_{II}$  is computed as:

$$A_{II} = \frac{1}{2}(\Delta\sigma')_{eq} = \frac{1}{2} \max_{t_0 \in D_t} \max_{t \in D_t} (\sigma(t) - \sigma(t_0))_{eq} \quad (26)$$

and the *mean hydrostatic stress* as:

$$\bar{\sigma}_H = \text{mean} \frac{1}{3} \text{tr} \boldsymbol{\sigma} = \frac{1}{6} \left( \max_{t \in D_t} \text{tr} \boldsymbol{\sigma}(t) + \min_{t \in D_t} \text{tr} \boldsymbol{\sigma}(t) \right) \quad (27)$$

with ‘tr’ the trace operator.

Following the same idea, Wöhler relations for predicting the number of cycles to rupture for triaxial loading can simply be adapted computing  $\mathcal{W}((\Delta\boldsymbol{\sigma}')_{eq}, 3\bar{\sigma}_H; \boldsymbol{\theta})$  using the functions  $\mathcal{W}$  and the parameters introduced and identified in section 3.1. Thereby, the triaxial extension of the model (9) proposed by [Chaboche and Lesne, 1988] yields:

$$N_R = \mathcal{W}(A_{II}, \bar{\sigma}_H; \boldsymbol{\theta}) = \frac{{}^*\sigma^U - A_{II}}{A_{II} - \sigma_0^\infty(1 - 3b\bar{\sigma}_H)} \left[ \frac{A_{II}}{B_0(1 - 3b\bar{\sigma}_H)} \right]^{-\beta} \quad (28)$$

and the relation (16) proposed in this work becomes:

$$N_R = \mathcal{W}(A_{II}, \bar{\sigma}_H; \boldsymbol{\theta}) = 10^{n_0 - \psi_c^{-1} \left( \tan \left( \frac{A_{II} - {}^*\sigma^U}{A} \right) + \tan^{-1}(-\psi_c(-n_0)) \right)} \quad (29)$$

with:

$$A = \frac{{}^*\sigma^U - \sigma_0^\infty(1 - 3\bar{\sigma}_H)}{\Pi/2 + \tan^{-1}(-\psi_c(-n_0))} \quad (30)$$

Note that nonlinear cumulative damage relation can also be obtained doing the same kind of substitution in equation (17). Also note that this relation was initially derived by [Chaudonneret, 1993] and has also been used by other authors for the study of Titanium alloys [Marmi et al., 2009]. Alternatively to what is proposed above, when comparing the stress state to the ultimate stress  $\sigma^U$ , the classical Von-Mises or Hill equivalent stresses can be used in eq. (28) (numerator) and for defining  $\alpha$  in (17).

**Remark.** Different lifetime predictions  $N_R$  for complex triaxial load cases can also be obtained involving different classical fatigue limit indicators such as Crossland or Dang-Van criteria instead of Sines criterion (25) used here.

One thus have a methodology capable of predicting the number  $N_R$  to rupture, a given elementary, non-necessarily sinusoidal triaxial stress-state (of support  $D_t$ ) can be repeated on a REV. Of course, in the perspective of counting the repetitions of this elementary loading, this latter should only be made of one simple pattern, that could be possibly assimilated to a ‘load cycle’. This last hypothesis might be too restrictive in real-life applications. Furthermore, the objective was precisely to avoid the too simplistic sinusoidal-like loading case.

Let us then assume that the loading to be repeated, called *Block* on Fig. 8, is composed of  $P$  elementary pattern called *Phases*.

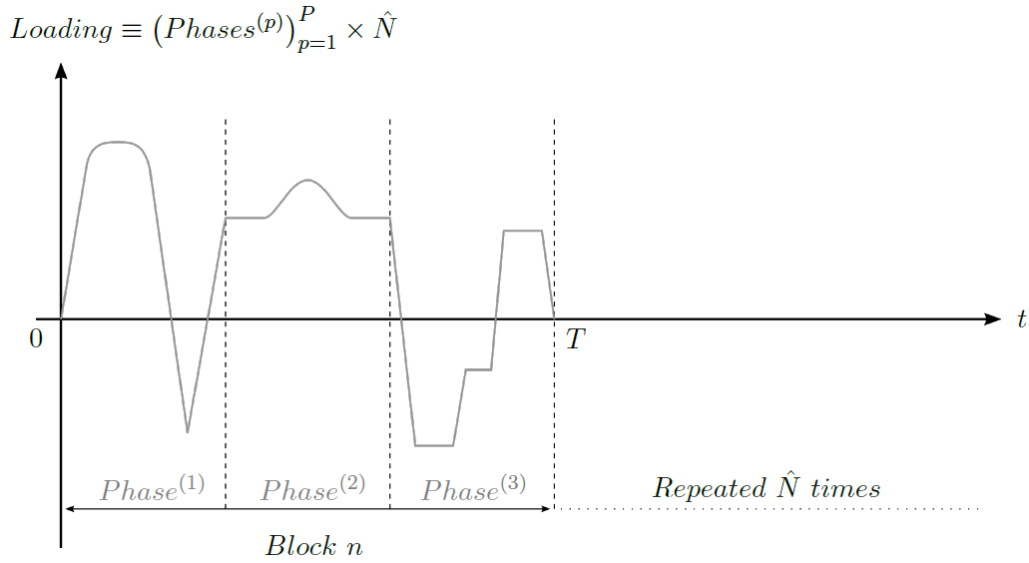


Fig. 8: Thermal loading #2 - Repetition of  $\hat{N}$  blocks composed of  $P$  known phases.

Let us recall that the loading in current approach is described by a vector  $f$  associated to different kinds of load factors (temperature fluctuations, nominal regime, boundary conditions variations in terms of flux or temperature accounting for valve opening, etc.) and that transient thermal variations leading to non-proportional stress-state can occur during those phases. Then, for each phase  $p$ , the stress state  $\sigma_g^{(p)}(t)$  in each Gauss point can be evaluated solving the associated linear thermo-mechanical FE problem and a corresponding number of cycles to failure  $N_{R,g}^{(p)} = \mathcal{W}(A_{II,g}^{(p)}, \bar{\sigma}_{H,g}^{(p)}, \theta)$  can be evaluated. Finally, the complete damage state at Gauss point  $g$ , accounting for the  $P$  consecutive phases, can be estimated using linear or nonlinear cumulative damage rules (see subsection 3.1) assuming that the block  $(Phases^{(p)})_{p=1}^P$  is repeated  $\hat{N}$  times. For example, when assuming linearly cumulative damage, for each Gauss point, the damage value is computed as:

$$d_g = \sum_{p=1}^P \frac{\hat{N}}{N_{R,g}^{(p)}} \tag{31}$$

Fig. 9 gives a graphical description of this second original approach for the computation of damage at the Gauss points level.

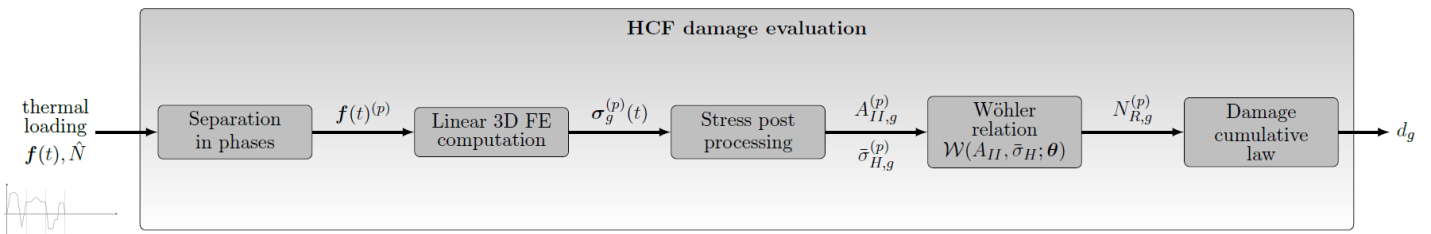


Fig. 9: Preliminary thermal loading - Approach #2 - Computation of  $d_g$  for each Gauss points.

### 3.4 Synthesis

In this section, two approaches have been proposed for the computation of the damage pattern after a nominal thermal loading (see Fig. 7 and Fig. 9). The duration of the loading itself is unknown and will be one of the demand parameters for the construction of the fragility curves. For this preliminary thermal study, the damage state  $d(x_g, t_s)$  of HCF origin in each Gauss point is computed from the knowledge of the stress distribution  $\sigma(x_g, t)$  given by a linear 3D FE calculation and after interpolation of reference Wöhler curves.

The predicted damage pattern  $d(x_g, t_s)$ , described as a lifetime ratio, must now be translated into an initial damage  $D(x_g, t_s)$  in conformity with the continuum damage mechanics framework. In what follows, as implicitly suggested by the work of [Chaboche and Lesne, 1988] and also described in [Lemaitre et al., 2009], a simple function  $\phi$  will be used for relating the two damage descriptions:

$$D = D_c \phi(d), \text{ with } \begin{cases} \phi(0) = 0 \\ \phi(1) = 1 \end{cases} \quad (32)$$

where  $D_c$  is the critical damage threshold. Fig. 3 gives an illustration of such a function choosing  $\phi(d) = d^\eta$ . An alternative choice, still guided by [Chaboche and Lesne, 1988], can be made writing  $\phi(d) = 1 - (1 - d^\eta)$ . In this work, for AISI 304L SS, no reference value for  $\eta$  could be identified due to lack of experimental data, but values within [3; 10] seem to be reasonable options.

Let one recall that the two damage descriptions are assembled in a unique comprehensive framework for conducting the seismic analysis but are nonetheless associated to different phenomena. In the HCF thermal phase, irreversibilities occur at the micro-scale for large load cycles as the material should behave in the elastic regime. Micro-cracks appear, grow and spread, but no plasticity at the meso-scale is involved. Thus, the seismic analysis of the structure detailed in following section 4 involves a nonlinear elastoplastic model for AISI 304L SS where damage growth is governed by plasticity at the meso-scale and the procedure is initialized considering, in each Gauss point, an initial damage value  $D(x_g, t_s) = D_c \phi(d(x_g, t_s))$  and identically null plasticity internal variables.

## 4 Nonlinear seismic response – Final damage pattern

This section details the dynamic nonlinear calculations to be conducted for seismic analysis under LCF assumption. Section 4.1, starts with the description of the elastoplastic model [Marquis, 1989, Chaboche, 1989, Lemaitre et al., 2009] used in conjunction with Lemaitre's damage evolution law governed by plasticity [Lemaitre and Desmorat, 2005], describing the constitutive material of the studied piping element. Section 4.2 gives details on the identification of the constitutive parameters for AISI 304L SS from the experimental references of Table 2. Finally, the nonlinear solver with MOR capabilities is briefly described in section 4.3.

### 4.1 Elastoplastic model including isotropic damage description

The model is expressed within the standard generalized material framework with internal variables describing the evolution of the elasticity/plasticity boundary and associated damage. One thus introduces the internal variables and their dual counterparts gathered in Table 5.

Table 5: Dual and primal internal variables used for LCF modeling.

Dual variables	Primal variables	Description
$\sigma$	$\epsilon^p$	Stress and plastic strain tensors
$\beta$	$\alpha$	Dual and primal kinematic hardening tensors
$R$	$r$	Dual and primal isotropic hardening tensors
$Y$	$D$	Elastic energy density and damage variable

In a Maxwell context, the elastic and plastic strain tensors, respectively  $\epsilon^e$  and  $\epsilon^p$ , verify:  $\epsilon = \epsilon^e + \epsilon^p$ . When damage occurs, as already introduced in (3), the effective stress on the REV becomes:

$$\tilde{\sigma} = \frac{\sigma}{1-D} \quad (33)$$

Alternatively, to account for crack closure phenomena, as introduced in [Bhattacharyya et al., 2019], the following definition can be used:

$$\tilde{\sigma} = \frac{\sigma'}{1-D} + \left[ \frac{\langle \sigma_H \rangle}{1-D} - \langle -\sigma_H \rangle \right] \mathbf{1} \quad (34)$$

where  $\langle \star \rangle = \max(\star, 0)$  extracts positive part. Elasticity relation using  $\tilde{\sigma}$  and classical Hooke's tensor  $\mathbb{E}$  writes:

$$\tilde{\sigma} = \mathbb{E} : \epsilon^e \quad (35)$$

and *elastic energy density*  $Y$  reads:

$$Y = \frac{1}{2} \epsilon^e : \mathbb{E} : \epsilon^e = \frac{1}{2} \tilde{\sigma} : \mathbb{E}^{-1} : \tilde{\sigma} = \tilde{R}_v \frac{(\tilde{\sigma})_{eq}^2}{2E} \quad (36)$$

using the triaxiality function  $\tilde{R}_v = \frac{2}{3}(1+\nu) + 3(1-2\nu)\langle \tilde{\sigma}_H / (\tilde{\sigma})_{eq} \rangle^2$  associated to effective stress.

The evolution of the elastic domain is described in the stress space, using kinematic and isotropic hardening variables  $\beta$  and  $R$ , by the means of the *plastic threshold function*:

$$f = \left( \frac{\sigma'}{1-D} - \beta \right)_{eq} - R(r) - \sigma^Y, \quad \text{with} \quad \begin{cases} f < 0 : \text{elasticity} \\ f \geq 0 : \text{plasticity} \end{cases} \quad (37)$$

where  $\sigma^Y$  is the yield threshold constant. Linear or nonlinear constitutive relations then link primal  $(\alpha, r)$  and dual  $(\beta, R)$  variables. For kinematic hardening, one considers:

$$\beta = \frac{2}{3} C \alpha \quad (38)$$

and for isotropic hardening, one of those classical relations can be used:

$$R(r) = K r^k \quad (39)$$

$$R(r) = R_\infty [1 - \exp(-\rho r)] \quad (40)$$

One then introduces the *potential dissipative function*  $F$  such as:

$$F = f + F_\beta + F_D \quad (41)$$

$F_\beta$  is a potential function needed for nonlinear kinematic hardening description which involves a new material parameter  $\gamma$  such that:

$$F_\beta = \frac{3\gamma}{4C} \beta : \beta \quad (42)$$

$F_D$ , in turn, is the *damage potential function* written after Lemaitre's damage evolution law and involving two new material parameters  $s$  and  $S$ :

$$F_D = \frac{S}{(s+1)(1-D)} \left(\frac{Y}{S}\right)^{s+1} \quad (43)$$

The evolution laws are then obtained by using the *normality rule* and introducing the *plastic multiplier*  $\lambda$ . The following relations can then be obtained:

$$\dot{\epsilon}^p = \lambda \frac{\partial F}{\partial \sigma} = \frac{\lambda}{1-D} \frac{\partial f}{\partial \tilde{\sigma}} = \frac{3\lambda}{2(1-D)} \frac{\tilde{\sigma} - \beta}{(\tilde{\sigma} - \beta)_{eq}} = \dot{p} \sqrt{\frac{3}{2}} \tilde{N} \quad (44)$$

$$\dot{r} = -\lambda \frac{\partial F}{\partial R} \Rightarrow \dot{r} = \dot{\lambda} \quad (45)$$

$$\dot{\alpha} = -\lambda \frac{\partial F}{\partial \beta} = \frac{3}{2} \lambda \left[ \frac{\tilde{\sigma} - \beta}{(\tilde{\sigma} - \beta)_{eq}} - \frac{\gamma}{C} \beta \right] \Rightarrow \dot{\alpha} = (1-D)(\dot{\epsilon}^p - \dot{p} \gamma \alpha) \quad (46)$$

where the *cumulative plastic strain*  $p$  is introduced and verifies:

$$\dot{p} = \sqrt{\frac{2}{3}} \dot{\epsilon}^p : \dot{\epsilon}^p = \frac{\lambda}{1-D} \sqrt{\frac{2}{3}} \frac{\partial f}{\partial \tilde{\sigma}} : \frac{\partial f}{\partial \tilde{\sigma}} \Rightarrow \boxed{\dot{\lambda} = (1-D)\dot{p}} \quad (47)$$

and using the *unit normal to plastic domain*  $\tilde{N}$  defined such as:

$$\tilde{N} = \sqrt{\frac{2}{3}} \frac{\partial f}{\partial \tilde{\sigma}} \quad (48)$$

The evolution of the damage variable, in turn, is governed by plasticity and is written according to Lemaitre's law:

$$\dot{D} = -\lambda \frac{\partial F_D}{\partial Y} \Rightarrow \begin{cases} \dot{D} = \dot{p} \left(\frac{Y}{S}\right)^s & \text{if } w \geq w_D \\ \dot{D} = 0 & \text{otherwise} \end{cases} \quad (49)$$

$$D = D_C \Rightarrow \text{meso-crack initiation}$$

In (49), the criterion for damage evolution is written on the *stored energy*  $w_S$  defined as:

$$w_S = \int_0^t (R\dot{r} + \boldsymbol{\beta} : \dot{\boldsymbol{\alpha}}) dt \quad (50)$$

Note that, according to e.g. [Lemaitre and Desmorat, 2005], for sinusoidal LCF load cases, an alternative criterion on plastic cumulative deformation  $p \geq p_D$  is generally used in (49). The criterion  $p_D$  in this case is application-dependent and is given in function of the applied loading  $(\Delta\boldsymbol{\sigma})_{eq} = \sigma_{eq,max} + \sigma_{eq,min}$ . For more complex inputs like seismic loading with richer non-steady state spectral content, the stored energy criterion must be used. In [Lemaitre and Desmorat, 2005] however, a *modified stored energy* is defined for writing the damage initiation criterion. Indeed, in order to prevent the isotropic term from soaring when performing time-integration and balancing the weight of the two isotropic- and kinematic-hardening terms, one considers:

$$\bar{w}_S = \int_0^t (R(r)z(r)\dot{r} + \boldsymbol{\beta} : \dot{\boldsymbol{\alpha}}) dt \quad (51)$$

with  $z(r) = Ar^m$  introducing two new material constants  $A$  and  $m$ . A complete illustration of the regular vs. modified stored energy behavior will be given later in section 4.2.2. Let just note that his change redefines two new thermodynamical internal variables  $(q, Q)$  verifying:  $Q(q) = R(r)$  and  $dq = z(r)dr$ .

The temporal resolution of these constitutive relations is performed using an adapted *radial return* algorithm (see e.g. [Simo and Hughes, 1998] for more details on such algorithm for plasticity).

## 4.2 Identification of material parameters

This subsection details how material parameters are identified for AISI 304L SS (THY) from experimental data contained in refs. of Table 2. Some material parameters, contained in Table 6, are well documented in many references and can be considered as reliably known.

Table 6: AISI 304L SS (THY) reliably known monotonic properties after [Colin et al., 2011; Kweon et al., 2021].

$E$	Young's modulus	$1.92 \times 10^5$ MPa
$\nu$	Poisson's ratio	0.3
$\sigma_{0,2}^Y$	Yield stress 0:2% offset	202 MPa
$\sigma^U$	Ultimate tensile strength	608 MPa
$\epsilon_D^p$	Uniform elongation (ultimate)	0.665
$\sigma_R$	Rupture tensile strength	288 MPa
$\epsilon_R^p$	Total elongation (rupture)	0.858
$Z$	Reduction in area (rupture)	0.864

Let one assume that the unknown parameters involved in the constitutive relations of section 4.1 are gathered in a vector  $\boldsymbol{\eta}$ . These parameters describing first plasticity and second, the

damage process, will be identified based on the tests-results set  $\mathcal{R} = \{T, C10, C1, C2\}$  of refs. in Table 2, where uniaxial deformation time histories  $\epsilon_{xx}(t)$  is imposed to material samples.

For each experiment  $r \in \mathcal{R}$ , one compares the model predictions  $\mathcal{M}(\epsilon_{xx}^r(\tau \leq t); \boldsymbol{\eta})$  with available stress measurement  $\sigma_{xx}^r(t)$  and build the cost function:

$$\mathcal{J}(\boldsymbol{\eta}) = \sum_{r=1}^{\text{card}\mathcal{R}} \sum_{t \in D_t^r} w_t^r \|\mathcal{M}(\epsilon_{xx}^r(\tau \leq t); \boldsymbol{\eta}) - \sigma_{xx}^r(t)\|^2 \quad (52)$$

taking into account the experimental database  $\mathcal{R}$  as a whole and introducing some weighting  $w^r$  for favoring the reproduction of the LCF tests  $C1$  and  $C2$ . The functional  $\mathcal{J}$  is then minimized w.r.t  $\boldsymbol{\eta}$  using classical *Nonlinear Least-Squares* (NLS) minimization techniques from initial guess  $\boldsymbol{\eta}_0$ . Model predictions associated to optimal values  $\hat{\boldsymbol{\eta}}$  are compared with reference experiments in Fig. 10.

Upcoming sections 4.2.1 and 4.2.2 discuss the results, detail identification when needed and give the values of the identified parameters.

#### 4.2.1 Parameters describing plasticity

In this subsection, only plasticity is considered, i.e. no damage is taken into account ( $D = 0$  in constitutive equations of subsection 4.1) and experimental curves  $\{T, C1, C2\}$  of Fig. 10 are cropped for isolating the pre-peak part.

A first minimization was launched following the lines and equations of section 4.1 (with constant  $C$  and  $\gamma$  parameters), enabling good reproduction of the cyclic test [C10]. However the tensile test [T] and cyclic responses [C1] and [C2] could not be satisfactorily reproduced. Let one notice that AISI 304L SS is known for presenting primary and secondary hardening, visible in Fig. 10 on [C1] and [C2]. In the uniaxial case, an analytical expression of the stress amplitude is given by:

$$\frac{\Delta\sigma}{2} = \frac{2C}{3\gamma} \tanh\left(\gamma \frac{\Delta\epsilon^p}{2}\right) + \sigma^Y + R(p) \quad (53)$$

Assuming that  $p \approx 2N\Delta\epsilon^p$ , one can readily see that only one hardening phenomenon can be reproduced by  $R(p)$  on the  $\Delta\sigma/2$  vs.  $N$  curves of Fig. 10a and b. Hence, in this work, as also suggested by [Lemaitre et al., 2009, p.226], we consider variable kinematic hardening coefficients  $C(p)$  and  $\gamma(p)$ , function of the cumulative plastic deformation  $p$ . The objective introducing a new dependence in  $p$  is to reproduce both primary and secondary hardening. The Armstrong-Frederick relation becomes:

$$\dot{\boldsymbol{\beta}} = \frac{2}{3} C(p) \dot{\epsilon}^p - \gamma(p) \dot{p} \boldsymbol{\beta} \quad (54)$$

From a thermodynamical point of view, the functions  $C(p)$  and  $\gamma(p)$  must respectively be increasing and decreasing functions. In this work, the following parametrization is adopted, to allow slow variations of the kinematic hardening parameters with respect to  $p$ :

$$C(p) = C_0 + \Delta C(1 - e^{-\kappa_C p}) \quad (55)$$

$$\gamma(p) = \gamma_\infty + \Delta\gamma e^{-\kappa_\gamma p} \quad (56)$$

Table 7 collects the parameters identified in the NLS sense choosing alternatively power and exponential law for  $R(p)$  and producing similar results. The plots of Fig. 10 are realized for parameters in the central column of Table 7 specifying power law for  $R(p)$ .

One can note here that the plastic part of the tensile curve [T] is fairly well reproduced and that both cyclic tests [C1] and [C2] show very good accordance with the experimental reference, modelling both primary and secondary hardening phenomena. On the 10 cycles

test [C10] however, even if extreme values of  $\sigma_{xx}$  are very satisfactory, one can observe on Fig. 10b that loops are only partially well reproduced with this set of parameters. One shall remark, that this difference will not change the extreme values of the kinematic hardening part of the stored energy which is written as a function of the maximum value of  $\beta$  on each cycle in the uniaxial case:

$$w_{s,kine} = \int_0^t \beta : \dot{\alpha} dt = \frac{4C}{3} \beta_{max}^2(t) \quad (57)$$

Hence, this will not affect the damage criterion too much, only within one cycle indeed, but not from cycles to cycles, since extreme values of  $\Delta\sigma/2$  and therefore  $\beta$  are well reproduced. Additional illustration of this claim is given in next section.

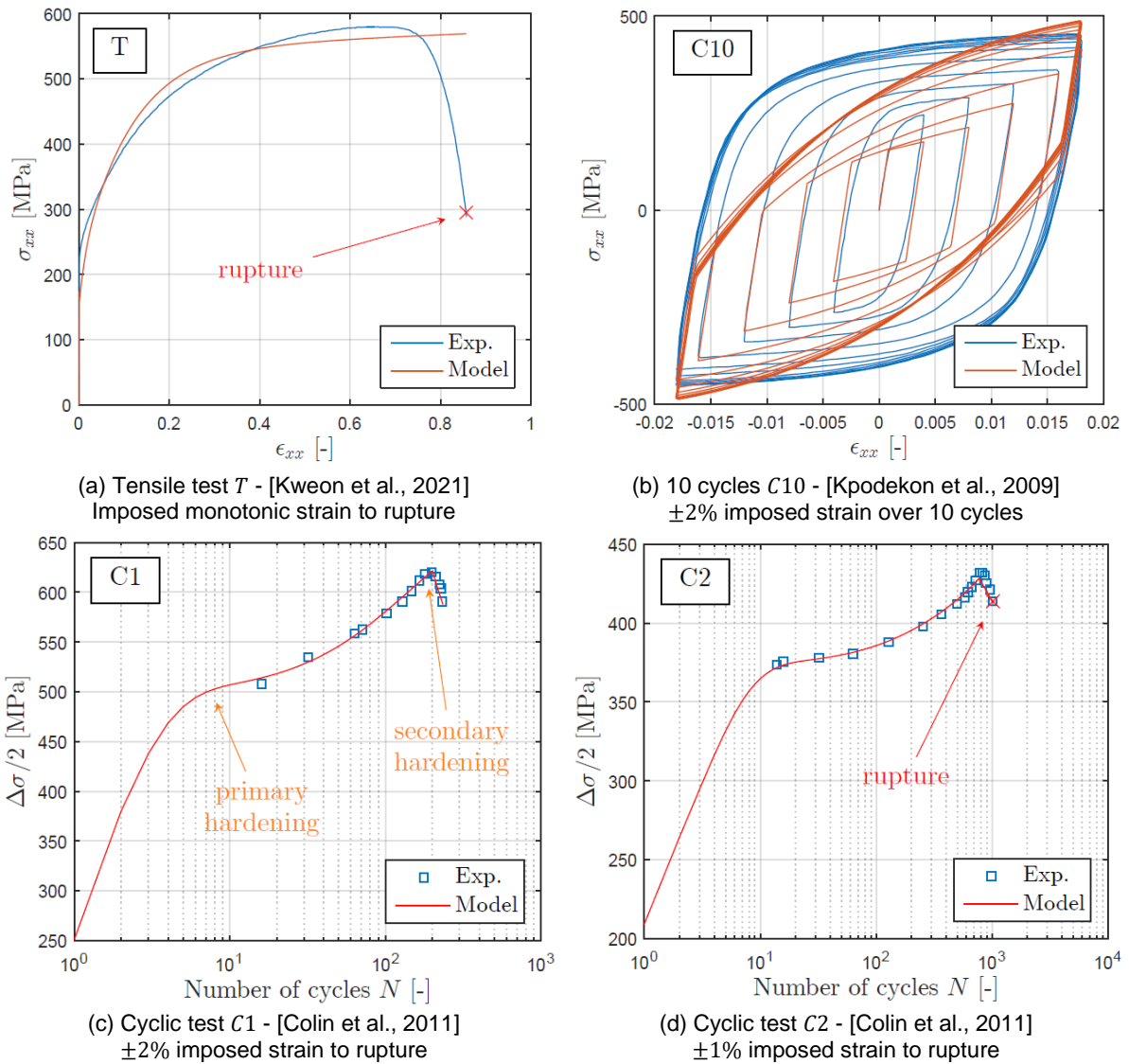


Fig. 10: Experimental results (blue curves) vs. best NLS fitted model predictions (red curves) for the four experimental refs. of Table 2.

Table 7: Optimal plasticity parameters for AISI 304L SS w.r.t. experimental refs. In Table 2 - Nonlinear kinematic hardening with variable  $\gamma(p)$  and  $C(p)$  - Power and exponential law for isotropic hardening.

Plasticity Parameters	Power law (39)	Exponential law (40)
$\sigma^Y$	154 MPa	181 MPa
Iso. Hard. constant	1.73 MPa ( $K$ )	$1.00 \times 10^3$ MPa ( $R_\infty$ )
Iso. Hard. exponent	0.9844 ( $k$ )	$1.88 \times 10^{-3}$ ( $\rho$ )
$C_0$	$1.15 \times 10^4$ MPa	$2.94 \times 10^3$ MPa
$\Delta C$	$3.50 \times 10^4$ MPa	$3.63 \times 10^4$ MPa
$\kappa_C$	8.958	12.8
$\gamma_\infty$	34.6	13.8
$\Delta\gamma$	44.6	56.1
$\kappa_\gamma$	0.121	0.105
<b>Relative LS error</b>	0.87%	1.66%

#### 4.2.2 Parameters describing damaging process

Now that the plastic part of the cyclic tests is correctly reproduced, a calibration of the threshold on the stored energy is needed for setting the start of the damaging phase. In this section, the plots refer to power law (39) for isotropic hardening. Fig. 11 shows a plot of the stored energy  $w_S(p)$  in its original version:

$$w_S = \underbrace{\int_0^t R \dot{r} dt}_{\text{isotropic hardening contribution}} + \underbrace{\int_0^t \boldsymbol{\beta} : \dot{\boldsymbol{\alpha}} dt}_{\text{kinematic hardening contribution}} \quad (58)$$

When performing the integration ( $r = p$  because no damage is involved in the pre-peak part), with a power law, the isotropic hardening term becomes:

$$w_{S,iso}(p) = \frac{K}{k+1} p^{k+1} \quad (59)$$

For kinematic hardening, one has:

$$w_{S,kine}(p) = \frac{4C}{3} \boldsymbol{\beta} : \boldsymbol{\beta} \quad (60)$$

which becomes a periodic function when  $\boldsymbol{\beta}$  saturates. One can clearly see on Fig. 11 that the stored energy is dominated by the isotropic hardening contribution (when compared to the kinematic hardening oscillatory part) to the point that no common damage initiation criterion can be written for the material using this definition.

As described in section 4.1, a change in variables is introduced to temperate the isotropic hardening contribution. The isotropic part of the stored energy then becomes for power law:

$$\bar{w}_{S,iso} = \int_0^t R(p) z(p) \dot{p} dt = \frac{KA}{k+m+1} p^{k+m+1} \quad (61)$$

With  $z(p) = Ap^m$ .

Let one introduce  $p_D^T = 0.665$ ,  $p_D^1 = 13.8$  and  $p_D^2 = 24.5$ , the cumulative plastic strains for which damage occurs for each of the three tests  $\{T, C1, C2\}$ . One now identifies the couple of coefficients  $(A, m)$  that enable (if possible) the same corrected stored energy for each test, i.e.  $\bar{w}_S(A, m, p_D^T) = \bar{w}_S(A, m, p_D^1) = \bar{w}_S(A, m, p_D^2)$ . NLS minimization is involved once again and Fig. 12 shows the results obtained with optimal parameters  $A = 0.7052$  and  $m = -1.574$ . One can

notice that the corrected stored energy now reaches similar values for tests [C1] and [C2] but the algorithm fails at identifying a pair  $(A, m)$  guaranteeing that the tensile test damages for similar level. One can note regarding this last observation, that the regimes are very different for tensile and cyclic tests. For tensile test, plastic strain value at the beginning of damage equals the cumulative plastic strain  $\epsilon_D^p = p_D^T = 0.665$ . The value 0.665 reached is huge for plastic strain but small for cumulative plastic strain compared to cyclic tests. The identified value does not enable to reproduce the damaging tensile test [T] (as can also be observed on Fig. 10a) but leads to appropriate threshold definition for high amplitude cyclic test, which is the range under focus for seismic analysis.

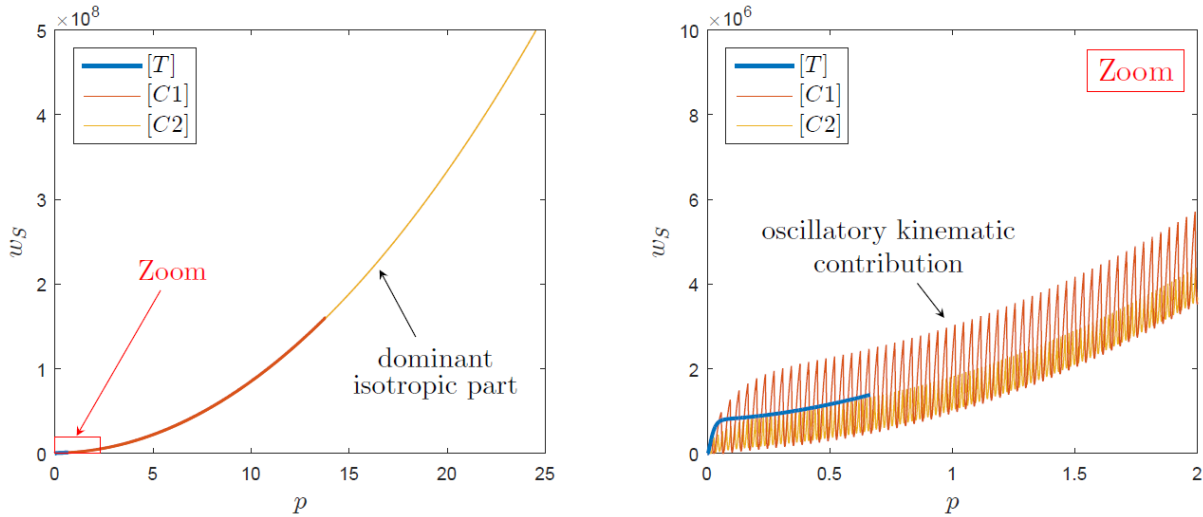


Fig. 11: Original stored energy  $w_s(p)$  (zoom on the right).

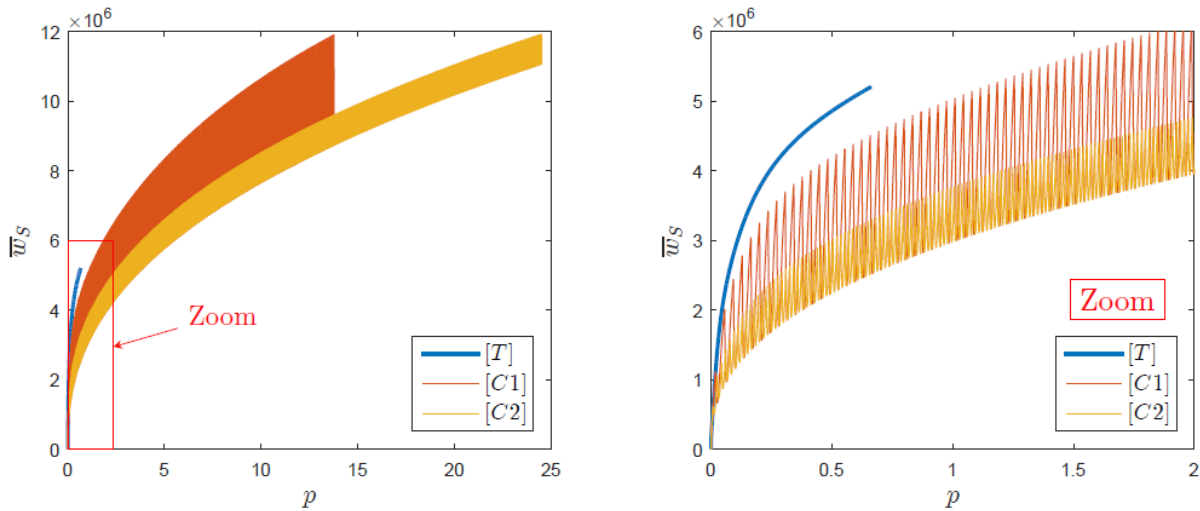


Fig. 12: Corrected stored energy  $\bar{w}_s(p)$  (zoom on the right).

One now needs to identify the parameters  $(s, S)$  of Lemaitre's damage law (49) from the damaging part (post-peak) of the cyclic tests. Several NLS minimization have been performed once again with different initial values leading this time to many correct and different optimal parameters in the sense of the NL cost-function involved. From the recommended value [Lemaitre and Desmorat, 2005] ( $s = 2, S = 2$  MPa), the optimal value ( $\hat{s} = 2, \hat{S} = 1.70$  MPa) was given by the algorithm. The reconstructed damaging part is visible on Fig. 10 and the parameters associated to damage evolution are collected in Table 8.

Let one note once again that the tensile test could not easily be reproduced with that set of values for  $(s, S)$  even if the values  $(A, m)$  were changed to more appropriate ones. Indeed, as

was said previously in this section, even if large  $\epsilon^p$  values are achieved, the cumulative plastic strain remains modest and would require respectively higher  $s$  and smaller  $S$  values for reproducing the damaging part of curve Fig. 10a. Tensile test, especially the damaging part where large deformation are expected, falls outside the scope of this study.

Table 8: Optimal damage parameters for AISI 304L SS with respect to experimental refs. In Table 2 – To be used with isotropic hardening power law (39).

$A$	0.7052
$m$	-1.574
$w_D$	11.9 MPa
$S$	1.7 MPa
$s$	2
<b>Relative LS error</b>	0.87%

### 4.3 The LATIN-PGD solver in a nutshell

Now that all material parameters have been identified, the nonlinear dynamics problem must be solved many times for different inputs and configurations. At this stage, one shall recall that the AISI 304L SS medium under study was submitted to a preliminary low level HCF loading of thermal origin that has led to a preliminary damage pattern in each Gauss point  $g$ . This preliminary pattern  $D(x_g, t_S)$  has been computed using one of the two approaches described in section 3 and making the classical distinction between micro-scale damage for low-level HCF loading where no meso-scale plasticity is involved, and meso-scale damage governed by plasticity. All the internal variables describing meso-scale plasticity will be considered identically null at time  $t_S$  when the seismic event occurs.

Let one thus consider the domain  $\Omega \in \mathbb{R}^3$  of Fig. 13, on the time domain  $I = [t_S, t_F]$ , with constant boundary  $\partial\Omega = \partial_N\Omega \oplus \partial_D\Omega$  over time and which behavior is described by the constitutive relations of subsection 4.1. This structure is submitted to surface forces  $f^N$  on  $\partial_N\Omega \times I$  (Neumann boundary conditions), to imposed displacements  $u^D$  on  $\partial_D\Omega \times I$  (Dirichlet boundary condition) and to volume forces  $f$  on  $\Omega \times I$ .

According to the internal variables of Table 5, required to describe the constitutive relations (damage governed by plasticity), the solution  $\mathcal{S}$  over the whole space-time domain  $I \otimes \Omega$  writes  $\mathcal{S} = (\mathbf{u}, \epsilon, \sigma, \epsilon^p, \beta, \alpha, Y, D)$ , where this condensed notation contains the values of the different solution fields at each point  $x$  of domain  $\Omega$  and each time  $t$  of  $I$ .

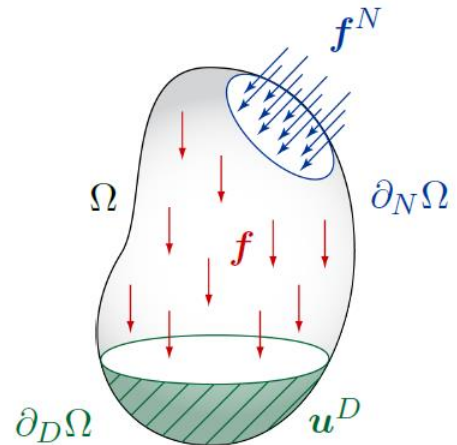


Fig. 13: The mechanical domain under study.

Unlike step-by-step methods, which seek the solution  $\mathcal{S}_{k+1}$  at time  $t_{k+1}$  from the knowledge of solution  $\mathcal{S}_k$  at time  $t_k$ , using a Newton-like algorithm to handle non-linearity and integration schemes (like Newmark scheme in dynamics) for time-integration, the LATIN method is an iterative solver that, from a kinematically and dynamically admissible initial elastic solution  $\mathcal{S}^{(0)}$ , consists in calculating successive nonlinear corrections until convergence is reached. Note that both initial solution  $\mathcal{S}^{(0)}$  and successive iterates  $\mathcal{S}^{(n)}$  are calculated over the whole time-space domain  $I \otimes \Omega$ . For this purpose, one defines an *admissibility space*  $\mathbf{Ad}$  where kinematic relations and loading boundary conditions are satisfied and a *manifold*  $\Gamma$  on which nonlinear

constitutive relations are verified. The sought solution  $\mathcal{S}$  lies at the intersection between both spaces  $\Gamma$  and  $\text{Ad}$ , as illustrated on Fig. 14.

From the initial admissible solution  $\mathcal{S}^{(0)} \in \text{Ad}$ , the LATIN method consists in finding the solution  $\mathcal{S} \in \Gamma \cap \text{Ad}$  in an iterative process composed of *nonlinear stages* (local in time and space), providing a prediction  $\hat{\mathcal{S}}^{(n+\frac{1}{2})} \in \Gamma$ , and *linear stages* (global over the whole space-time domain), providing an approximation  $\mathcal{S}^{(n+1)} \in \text{Ad}$ . The iterative search, starting from the elastic solution  $\mathcal{S}^{(0)}$ , can be summarized by writing:

$$\mathcal{S}^{(0)} \in \text{Ad} \cdots \rightarrow \mathcal{S}^{(n)} \in \text{Ad} \rightarrow \hat{\mathcal{S}}^{(n+\frac{1}{2})} \in \Gamma \rightarrow \mathcal{S}^{(n+1)} \in \text{Ad} \cdots \rightarrow \mathcal{S} \in \Gamma \cap \text{Ad} \quad (62)$$

The jumps from one subspace to the other are enabled by search directions  $\mathbb{G}$  and  $\mathbb{A}$  as illustrated on Fig. 14. These search directions are parameters of the LATIN method but standard stiffness operators are classically involved. Many more details on the methodology can be found in [Ladevèze, 1999].

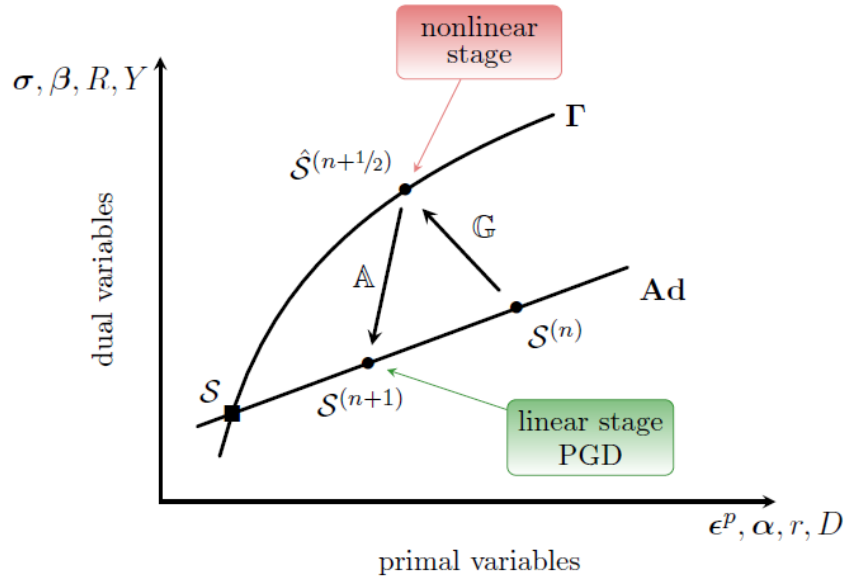


Fig. 14: Iterative resolution with search directions  $\mathbb{G}$  and  $\mathbb{A}$ .

Let one here mention that the *nonlinear or local stage* requires the simulation of the nonlinear constitutive relations (see section 4.1) for each time  $t$  and each Gauss point  $x_g$  in space. However, the computation of the primal and dual solution fields of  $\hat{\mathcal{S}}^{(n+\frac{1}{2})}$  for each  $(x_g, t)$  can be done in a parallel manner. At the *linear stage*, in turn, the admissibility relations (dynamic equilibrium of the structure) must be re-imposed on the whole time-space domain.

From the knowledge of  $\mathcal{S}^{(n)}$  and  $\hat{\mathcal{S}}^{(n+\frac{1}{2})}$ , the linearity of this global problem enables one to seek the solution increment  $\Delta\mathcal{S}^{(n)} = \mathcal{S}^{(n+1)} - \mathcal{S}^{(n)}$  as a *low rank approximation* using the *Proper Generalized Decomposition* (PGD).

Without going into more details, let one simply mention that, similarly to what can be done in dynamics when projecting equilibrium equations onto a truncated modal basis, the primal and dual fields of  $\Delta\mathcal{S}^{(n)}$  are computed on a reduced basis composed of modes defined as a product of temporal and spatial functions. During the first iterations of the LATIN algorithm, new PGD modes must be computed, but, as the solver progresses, the systematic enrichment of the basis might not be needed anymore at the linear stage; in that case, the linear stage simply consists in computing temporal corrections on a truncated basis. More details about the PGD itself and the different possible implementation for transient problems can be found in [Nouy, 2010] and many numerical applications of the PGD within the LATIN framework can be found

e.g. in [Relun et al., 2013; Néron et al., 2015; Heyberger et al., 2012; Vitse et al., 2019]. Let one also mention the recent application of the LATIN-PGD methodology in dynamics during the doctoral work of Sebastian Rodriguez-Iturra, (NARSIS WP4).

Thus, the LATIN framework, with embedded PGD as model order reduction tool, enables to exploit the redundancy of information contained in transient solutions and is particularly suited for solving parametric problems. Indeed, let one assume that the problem is described with a given number of parameters contained in a vector  $\boldsymbol{\eta}$ . More precisely, consider the case where one seeks a set of solutions  $\{\mathcal{S}_1, \dots, \mathcal{S}_{np}\}$  for a given previously defined parameter set  $\{\boldsymbol{\eta}_1, \dots, \boldsymbol{\eta}_{np}\}$  assumed to have ‘reasonably close’ values from one  $\boldsymbol{\eta}_i$  to another  $\boldsymbol{\eta}_{i+1}$ . These parameters may be associated to the constitutive relations (manifold  $\Gamma$ ) or to the loading (Admissibility Ad). Fig. 15 gives a graphical illustration of both cases.

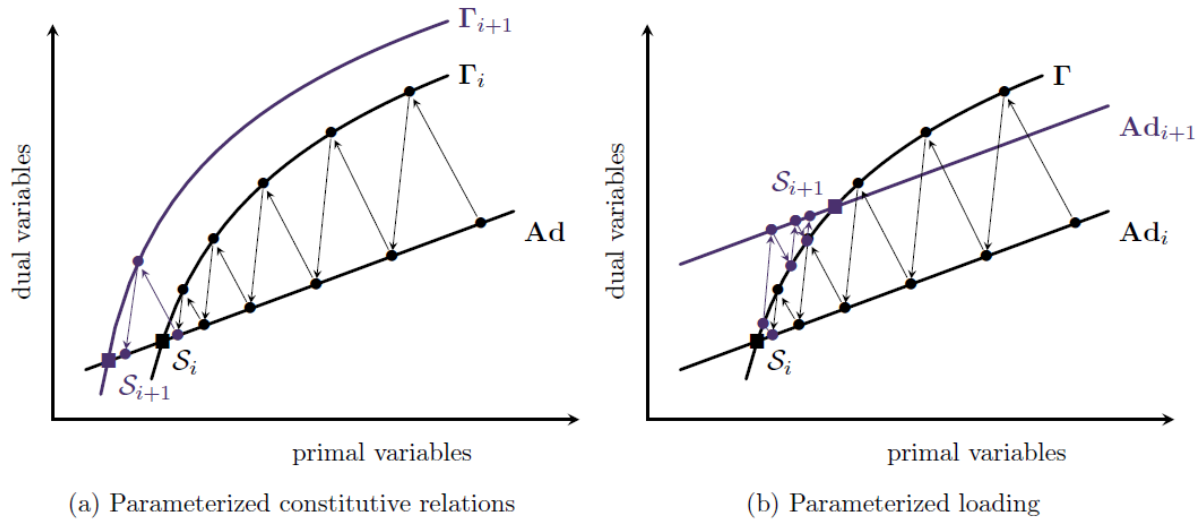


Fig. 15: Iterative strategy used for handling parametric dependency.

An efficient strategy can be defined for dealing with this kind of parametric dependency. Assuming that a set of solutions  $\{\mathcal{S}_1, \dots, \mathcal{S}_i\}$  is already computed, if the two vectors  $\boldsymbol{\eta}_i$  and  $\boldsymbol{\eta}_{i+1}$  (describing e.g. nonlinear part of constitutive relations) are sufficiently close, the associated spaces  $\Gamma_i$  and  $\Gamma_{i+1}$  will also be close. So, rather than initializing the solution  $\mathcal{S}_{i+1}$  to the space-time solution of the equivalent elastic problem as the classical LATIN approach suggests it, the already converged solution  $\mathcal{S}_i$  can advantageously be chosen as starting point. The advantage of this approach is twofold: if  $\Gamma_i$  and  $\Gamma_{i+1}$  are close to each other, the number of iterations for computing  $\mathcal{S}_{i+1}$  from  $\mathcal{S}_i$  is drastically reduced (see Fig. 15a) and the set of PGD modes computed at previous steps can be reused. The same strategy can of course be adopted if parameters describe the loading (see Fig. 15b).

## 5 Synthesis of the approach – Fragility curves

Now going back to our problem, for building the fragility curves, one needs to compute the probability  $\mathcal{P}(\|D\|_\infty \geq \bar{D}; a, \hat{N})$ , called *probability of failure*, that the maximum damaged area value  $\|D\|_\infty$  exceeds a given threshold  $\bar{D}$  and this, for a given acceleration level  $a$  and after  $\hat{N}$  repetitions of a nominal loading. Note that the threshold  $\bar{D}$  might be different from the limit damage value  $D_c$  introduced previously and which corresponds to the appearance of meso-cracks. For nuclear engineering application and safety analysis, a more conservative (lower) value might be chosen.

The knowledge of a given seismic scenario (magnitude, distance-to-source, local shear wave velocity, etc.) leads to a collection of likely seismic inputs to apply to the structure or component under study. The literature for generating potential seismic inputs from seismic scenario is vast [Douglas and Aochi, 2008; Charbonnel, 2018] and can be based on regression techniques on complete seismic database (see e.g. NGA-PEER Database [Power et al., 2008; Chiou and Youngs, 2008; Baker and Jayaram, 2008; Boore and Atkinson, 2008; Abrahamson and Silva, 2008] in California or RESORCE Database [Akkar et al., 2014] in Europe), on single recordings or spectral specifications (see e.g. [Rezaeian and Der Kiureghian, 2008; Rezaeian and Der Kiureghian, 2010; Lancieri et al., 2012; Yamamoto and Baker, 2011; Zentner et al., 2013; Rossetto et al., 2016; Lancieri et al., 2018]) or on full physics-based propagation modelling (see e.g. [Zerva, 1988; Gatti et al., 2018]). To account for the huge variability of the possible ground motion inputs and according to the different earthquake resistant design recommendations for civil constructions [EUROCODE-8, 2004; Bisch et al., 2012; Elghazouli, 2009; NEHRP, 2010], numerical models, together with their own uncertainties (material parameters), must be subjected, not only to a single seismic loading, but to a set of potential seismic inputs (see Fig. 16). Hence, the fragility curves imply the computation of quasi-identical nonlinear solutions  $\mathcal{S}_i$  associated to different input realizations  $a_i(t)$  and thermal loading repetitions  $\hat{N}_i$ . As was already highlighted in the end of the previous subsection 4.3, the LATIN solver brings a particularly efficient framework for chaining the calculations, taking advantage of already computed PGD basis and similar solutions for initialization. The proposed strategy is graphically summed up on Fig. 16.

Let one finally note that the sequencing of the computations within the LATIN-PGD framework can have a determinant impact on the final computational cost for obtaining the fragility curves. Indeed, nonlinear solutions in dynamics  $\mathcal{S}_i$  will be similar if the seismic inputs  $a_i(t)$  are similar. In [Charbonnel, 2018], a two-stages strategy was proposed for modelling acceleration time-histories  $a_i(t)$  using a given reduced number of parameters (of the order of twenty) arranged in a vector  $\xi$ . Signal envelope and time-frequency content are simultaneously modelled using respectively univariate and bivariate log-normal distributions as illustrated in Fig. 17. Of course, an infinity of temporal realizations can be generated for a given  $\xi$ , but they all lead to similar pseudo-spectral accelerations as exemplified in the above mentioned reference. One can therefore assume that two signals  $a_i(t)$  and  $a_j(t)$  with close parameters values  $\xi_i$  and  $\xi_j$ , once filtered by the (nonlinear) structure, will lead to close solutions  $\mathcal{S}_i$  and  $\mathcal{S}_j$ . This parametrization can thus be used for a clever sequencing of computations resorting for example to kPCA-based clustering techniques.

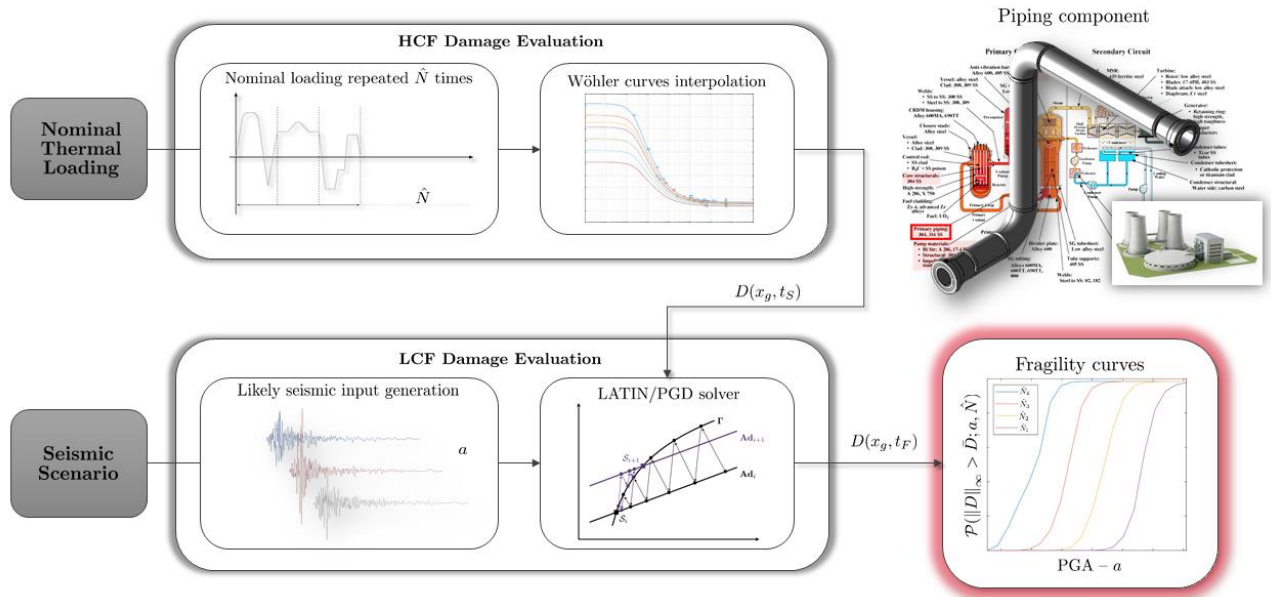


Fig. 16: Synthesis - Computation of fragility curves including nominal thermal ageing.

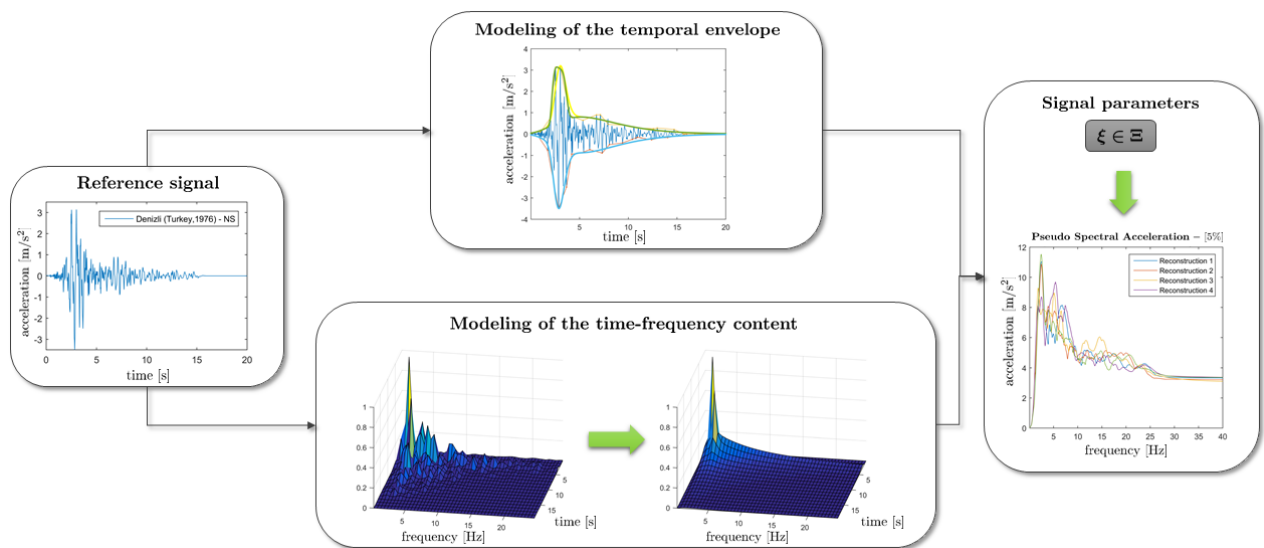


Fig. 17: Signal modelling procedure proposed in [Charbonnel, 2018].

## 6 Conclusions

In this contribution, a novel strategy was presented for computing fragility curves including both external seismic input motion and nominal thermal loading duration accounting for the unknown time of occurrence of the potential earthquake event. The study is carried out on metallic materials in an original HCF/LCF framework. One of the principal achievement of this work, besides the derivation of the general methodology, is the identification of the material parameters associated to AISI 304L stainless steel, of which many NPP sensitive elements are made. Thus, Wöhler curve description in the HCF range and elastoplastic model according to the standard generalized material framework in the LCF range have been identified. The identified optimal parameters strongly depend on the (few) available test results that could be consulted as experimental reference. However, these parameters enabled to reproduce a wide range of tests. Furthermore, the proposed strategy would be perfectly adapted to different class of steels and other types of metals: preliminary identification should simply be required.

Both approaches proposed for HCF enable to handle complex triaxial stress-state for metals and an empirical law is proposed for associating damage under the form of a lifetime ratio, to damage following the continuum damage mechanics framework. The LATIN-PGD method finally constitutes a favorable framework for the computation of the fragility curves combining both thermal HCF load duration and seismic loading. Clever initialization of the many solutions to compute, combined with efficient PGD reduced basis, make it a key asset for the computation of this numerical chart. More details and applications of this method can be found in [Rodriguez-Iturra, 2021] and in NARSIS deliverable D4.3. [Charbonnel 2022].

## 7 References

- Abrahamson, N. and Silva, W. (2008). Summary of the Abrahamson & Silva NGA Ground-Motion Relations. *Earthquake Spectra*, **24(1)**: 67-97.
- Akkar, S., Sandikkaya, M. A., Senyurt, M., Azari Sisi, A., Ay, B. O., Traversa, P., Douglas, J., Cotton, F., Luzi, L., Hernandez, B., and Godey, S. (2014). Reference database for seismic ground-motion in Europe (RESORCE). *Bull. Seism. Soc. America*, **12**: 311-339.
- Alameddin, S., Bhattacharyya, M., Fau, A., Nackenhorst, U., Néron, D., and Ladevèze, P. (2017). Large time increment approach for fatigue damage computations. *PAMM*, **17(1)**: 231-232.
- Arzt, M. (1994). Approche des phénomènes cycliques par la méthode à grand incrément de temps. PhD thesis, École Normale Supérieure de Cachan.
- Baker, J. W. and Jayaram, N. (2008). Correlation of Spectral Acceleration Values from NGA Ground Motion Models. *Earthquake Spectra*, **24(1)**: 299-317.
- Bhattacharyya, M., Fau, A., Desmorat, R., Alameddin, S., Néron, D., Ladevèze, P., and Nackenhorst, U. (2019). A kinetic two-scale damage model for highcycle fatigue simulation using multi-temporal latin framework. *European Journal of Mechanics-A/Solids*, **77**: 103808.
- Bhattacharyya, M., Fau, A., Nackenhorst, U., Néron, D., Ladevèze, P. (2018a). A model reduction technique in space and time for fatigue simulation. In *Multiscale modeling of heterogeneous structures*, pages 183-203. Springer.
- Bhattacharyya, M., Fau, A., Nackenhorst, U., Néron, D., Ladevèze, P. (2018b). A multi-temporal scale model reduction approach for the computation of fatigue damage. *Computer Methods in Applied Mechanics and Engineering*, **340**: 630-656.
- Bisch, P., Carvalho, E., Degee, H., Fajfar, P., Fardis, M. N., Franchin, P., Kreslin, M., Pecker, A., Pinto, P., Plumier, A., Somja, H., and Tsionis, G. (2012). Eurocode 8: Seismic Design of Buildings - Worked examples. In Acun, B., Athanasopoulou, A., Pinto, A., Carvalho, E., and Fardis, M., editors, *Worked examples presented at the Workshop "EC 8: Seismic Design of Buildings"*, Lisbon, 10-11 Feb. 2011, number EUR 25204 EN - 2012.
- Boore, D. and Atkinson, G. (2008). Ground-Motion Prediction Equations for the Average Horizontal Component of PGA, PGV, and 5%-Damped PSA at Spectral Periods between 0.01 s and 10.0 s. *Earthquake Spectra*, **24(1)**: 99-138.
- Chaboche, J.-L. (1989). Constitutive equations for cyclic plasticity and cyclic viscoplasticity. *International Journal of Plasticity*, **5**: 247-302.
- Chaboche, J. L. and Lesne, P. M. (1988). A non-linear continuous fatigue damage model. *Fatigue & Fracture of Engineering Materials & Structures*. **11(1)**:1-17
- Charbonnel, P.-E. (2018). Analyse temps-fréquence de signaux sismiques : différentes approches et tentatives de modélisation. (CEA) Technical report, DEN/DANS/DM2S/SEMT/EMSI/NT/2018-62544/A.
- Charbonnel, P.-E. (2022). PhD narrative on a model reduction strategy for complex, highly nonlinear and dynamic systems, based on the Proper Generalized Decomposition and LATIN approaches. NARSIS Deliverable D4.3.
- Chaudonneret, M. (1993). A simple and efficient multiaxial fatigue damage model for engineering applications of macro-crack initiation. *J. Eng. Mater. Technol.*, **115**: 373-379.
- Chiou, B. and Youngs, R. (2008). An NGA Model for the Average Horizontal Component of Peak Ground Motion and Response Spectra. *Earthquake Spectra*, **24(1)**: 173-215.
- Cognard, J.-Y. and Ladevèze, P. (1993). A large time increment approach for cyclic viscoplasticity. *International Journal of Plasticity*, **9(2)**: 141-157.

- Colin, J., Fatemi, A., and Said, T. (2011). Cyclic hardening and fatigue behavior of stainless steel 304L. *Journal of Materials Science*, **46**: 145-154.
- Dang Van, K. and Paradopoulos, I. V., editors (1999). *Highcycle metal fatigue : from theory to applications*. Springer, Wien New York.
- Douglas, J. and Aochi, H. (2008). A survey of techniques for predicting earthquake ground motions for engineering purposes. *Surveys in Geophysics*, **29**: 187-220.
- Elghazouli, A. Y., editor (2009). *Seismic Design of Buildings to EUROCODE 8*. Taylor and Francis.
- EUROCODE-8 (2004). Eurocode 8: Design of structures for earthquake resistance - part 1: General rules, seismic actions and rules for buildings. Technical Report EN 1998-1: 2004 (E), European Committee for Standardization, Management Centre: rue de Stassart, 36 B-1050 Brussels.
- Gatti, F., Touhami, S., Lopez-Caballero, F., Paolucci, R., Clouteau, D., Fernandes, V. A., Kham, M., and Voltaire, F. (2018). Broad-band 3-d earthquake simulation at nuclear site by an all-embracing source-to-structure approach. *Soil Dynamics and Earthquake Engineering*, **115**: 263-280.
- Heyberger, C., Boucard, P.-A., and Neron, D. (2012). Multiparametric analysis within the proper generalized decomposition framework. *Computational Mechanics*, **49**: 277-289.
- Kpodekon, C., Taleb, L., and Taheri, S. (2009). Etude de l'effet d'un pré-écrouissage sur la durée de vie d'un acier inoxydable austénitique 304L. In *19<sup>ème</sup> Congrès Français de Mécanique*, Marseille, France.
- Kweon, H. D., Kim, J. W., Song, O., and Oh, D. (2021). Determination of true stress-strain curve of type 304 and 316 stainless steels using a typical tensile test and finite element analysis. *Nuclear Engineering and Technology*, **53(2)**: 647-656.
- Ladevèze, P. (1985). Sur une famille d'algorithmes en mécanique des structures. *Comptes-rendus des séances de l'Académie des sciences. Série 2, Mécanique-physique, chimie, sciences de l'univers, sciences de la terre*, **300(2)**: 41-44.
- Ladevèze, P. (1999). *Nonlinear Computational Structural Mechanics*. Springer, NY.
- Lancieri, M., Bazzurro, P., and Scotti, O. (2018). Spectral matching in time domain: A seismological and engineering analysis. *Bull. Seism. Soc. America*, **108(4)**: 1972-1994.
- Lancieri, M., Madariaga, R., and Bonilla, F. (2012). Spectral scaling of the aftershocks of the Tocopilla 2007 earthquake in northern Chile. *Geophysical Journal International*, **189(1)**: 469-480.
- Lee, Y.-L., Barkey, M. E., and Kang, H.-T. (2011). *Metal Fatigue Analysis Handbook: Practical Problem-Solving Techniques for Computer-Aided Engineering*. Butterworth Heinemann.
- Lee, Y.-L. and Tjhung, T. (2011). Chapter 3 - Rainflow Cycle Counting Techniques. In Lee, Y.-L., Barkey, M. E., and Kang, H.-T., editors, *Metal Fatigue Analysis Handbook*, pages 89-114. Butterworth-Heinemann, Boston.
- Lemaitre, J., Chaboche, J.-L., Benallal, A., and Desmorat, R. (2009). *Mécanique des matériaux solides*. Sciences sup. Dunod, Paris, 3<sup>e</sup> édition.
- Lemaitre, J. and Desmorat, R. (2005). *Engineering damage mechanics*. Springer-Verlag Berlin Heidelberg.
- Marmi, A. K., Habraken, A. M., and Duchene, L. (2009). Multiaxial fatigue damage modelling at macro scale of Ti-6Al-4V alloy. *International Journal of Fatigue*, **31**:2031-2040.
- Marquis, D. (1989). *Phénoménologie et thermodynamique : couplages entre thermoélasticité, plasticité, vieillissement et endommagement*. PhD thesis, Université Paris IV.

- NEHRP (2010). Earthquake-resistant design concepts an introduction to the nehrp recommended seismic provisions for new buildings and other structures. Technical Report FEMA P-749, National Institute of Building Sciences, Building Seismic Safety Council Washington, DC. Prepared for the Federal Emergency Management Agency of the U. S. Department of Homeland Security By the National Institute of Building Sciences Building Seismic Safety Council.
- Nouy, A. (2010). A priori model reduction through proper generalized decomposition for solving time-dependent partial differential equations. *Comput. Methods Appl. Mech. Engrg.*, **199(23-24)**: 1603-1626.
- Néron, D., Boucard, P.-A., and Relun, N. (2015). Time-space PGD for the rapid solution of 3D nonlinear parametrized problems in the many-query context. *Int. J. Num. Methods in Engineering*, **103(4)**: 275-292.
- Pedersen, M. M. (2018). *Introduction to metal fatigue*. Techreport ME-TR-11, Department of Engineering, Aarhus University, Denmark.
- Poulain, T. (2015). *Fatigue oligocyclique d'un acier inoxydable austénitique 304L : influence de l'état de surface et de signaux de chargement en milieu eau primaire REP*. PhD thesis, ISAE-ENSMA Ecole Nationale Supérieure de Mécanique et d'Aérotechnique - Poitiers, Poitiers, France.
- Power, M., Chiou, B., Abrahamson, N., Bozorgnia, Y., Shantz, T., and Roblee, C. (2008). An overview of the nga project. *Earthquake Spectra*, **24(1)**: 3-21.
- Relun, N., Néron, D., and Boucard, P.-A. (2013). A model reduction technique based on the PGD for elastic-viscoplastic computational analysis. *Comput. Mechanics*, **51**: 83-92.
- Rezaeian, S. and Der Kiureghian, A. (2008). A stochastic ground motion model with separable temporal and spectral nonstationarities. *Earthq. Eng. Struct. Dyn.*, **37**: 1565-1584.
- Rezaeian, S. and Der Kiureghian, A. (2010). Simulation of synthetic ground motions for specified earthquake and site characteristics. *Earthq. Eng. Struct. Dyn.*, **39**: 1155-1180.
- Rodriguez-Iturra S. (2021). Virtual charts for earthquake engineering including loading parameters. PhD Thesis, Ecole Normale Paris-Saclay, France. <https://tel.archives-ouvertes.fr/tel-03446766/document>
- Rossetto, T., Gehl, P., Minas, S., Galasso, C., Dufour, P., Douglas, J., and Cook, O. (2016). Fracas: A capacity spectrum approach for seismic fragility assessment including record-to-record variability. *Engineering Structures*, **125**: 337-348.
- Simo, J. C. and Hughes, T. J. R. (1998). *Computational Inelasticity*, volume 7 of *Interdisciplinary Applied Mathematics*. Springer.
- Sines, G. (1959). *Behavior of Metals under Complex Static and Alternating Stresses*. McGraw-Hill, New York, NY, USA,.
- Vincent, L., Le Roux, J.-C., and Taheri, S. (2012). On the high cycle fatigue behavior of a type 304L stainless steel at room temperature. *International Journal of Fatigue*, **38**: 84-91.
- Vitse, M., Boucard, P.-A., and Néron, D. (2019). Dealing with a nonlinear material behavior and its variability through PGD models: Application to reinforced concrete structures. *Finite Elements in Analysis and Design*, **153**: 22-37.
- Yamamoto, Y. and Baker, J. W. (2011). Stochastic model for earthquake ground motion using wavelet packets. *Bull. Seism. Soc. America*, **103(6)**.
- Zentner, I., D'Amico, L., and Cacciola, P. (2013). Simulation of non stationary ground motion compatible with nga-spectra. In Deodatis, G., Ellingwood, B. R. and Frangopol, D. M., editors, *Safety, Reliability, Risk and Life-Cycle Performance of Structures and Infrastructures*, pages 2349-2355.

Zerva, A. (1988). Seismic source mechanisms and ground motion models. *Probabilistic Engineering Mechanics*, **3(2)**: 64-74.